ELSEVIER

Journal of Structural Geology 28 (2006) 2123–2143

JOURNAL OF STRUCTURAL GEOLOGY

www.elsevier.com/locate/jsg

Propagation of normal faults to the surface in basalt, Koae fault system, Hawaii

Stephen J. Martel*, Jason S. Langley

Department of Geology and Geophysics, University of Hawaii, 2525 Correa Road, Honolulu, HI 96822, USA

Received 9 September 2004; received in revised form 15 July 2005; accepted 6 December 2005
Available online 24 January 2006

Abstract

Normal fault scarps of the Koae fault system on Kilauea volcano consistently display locally breached monoclines underlain by prominent cavities, deep gaping fissures on the footwall, finer fissures on the hanging wall, and buckles at the scarp base. Elastic analyses reveal that this assemblage forms as a fault propagates up towards the surface rather than down from it. Models of a planar blind normal fault with a dip exceeding 60° yield a monocline with a tensile stress concentration at the surface where gaping fissures occur, a stronger subsurface tensile stress concentration near the blind fault tip, where cavities occur, and a compressive stress concentration at the surface where buckles occur. The footwall fissures grow down from the tensile stress concentration at the surface and link with a fault as its scarp grows. In contrast, the cavities initiate at depth near the fault tip and propagate with it up towards the surface. The hanging wall fissures apparently open in response to slip on late-forming blind antithetic faults near the surface. Stoped blocks derived from footwall fissure walls help prop the footwall fissures open as a normal fault breaches the surface. The fissures, cavities, and scarp rubble provide highly conductive hydraulic pathways.

Keywords: Faults; Fractures; Mechanics; Basalt; Hydrogeology

1. Introduction

Normal faults in basalt characterize oceanic and continental rifts on Earth and are common on other planets, but relatively few studies have focused on how normal faults propagate in basalt. We address this issue here. Normal faults in basalt and other layered volcanic rocks are of both academic and practical interest, for they commonly are involved in hydrothermal and geothermal systems (e.g. Bailey et al., 1976; Duffield et al., 1980; Carillo, 1998; Singleton and Criss, 2002; Kelley et al., 2002) and they influence fluid flow and contaminant transport at several federal facilities in the western United States (e.g. Ferrill and Morris, 2001; Link and Mink, 2002; Wilson et al., 2003). The significance of normal faults in a host of scientific and engineering matters on Earth, and the relative scarcity of studies on how normal faults propagate in basalt, both serve to motivate this study.

The propagation of normal faults in basalt is also of interest to planetary geologists. Planetary surfaces known or inferred to consist of basalt display normal faults on Mars (Bandfield et al., 2000; Christensen et al., 2003; Wilkens and Schultz, 2003), Venus (Head et al., 1992; Solomon et al., 1992), and the Moon (Guest and Greeley, 1977; Golumbek, 1979; Head and Wilson, 1993; Hiesinger et al., 2003). Normal faults also occur on Mercury, although whether they occur in ejecta from impact basins or lava flows is a matter of debate (Strom, 1987). Normal faults on Mars have been associated with overlying features, such as pit crater chains (Ferrill et al., 2004) and underlying features, such as dikes (e.g. Schultz et al., 2004). Normal faults also have been used to infer lithospheric thickness (e.g. Solomon et al., 1992). Since close-up observations of extraterrestrial faults are lacking, well-founded Earth analogs play a key roll in interpreting remote sensing imagery and topographic data to infer how the normal faults

* Corresponding author. Tel.: +1 808 956 7797; fax: +1 808 956 5154.
E-mail address: smartel@hawaii.edu (S.J. Martel).

0191-8141/$ - see front matter © 2005 Elsevier Ltd. All rights reserved.
doi:10.1016/j.jsg.2005.12.004

develop on other planets (e.g. Ferrill et al., 2004; Schultz et al., 2004).

Our focus is on the mechanics of normal fault propagation along dip rather than along fault strike (Kaven (2004) addresses the latter topic). The literature on normal fault propagation along dip is dominantly theoretical (e.g. Lin and Parmentier, 1988; Gudmundsson, 1992; Bruhn and Schultz, 1996; Willemse et al., 1996; Willemse, 1997; Cooke and Pollard, 1997; Crider and Pollard, 1998; Kattenhorn and Pollard, 1999), and it does not point to a clear mechanical tendency for a normal fault to propagate up towards the surface or down from it. Here we blend geologic field observations of surface deformation with mechanical analyses to address fault propagation; our approach parallels that used by Grant and Kattenhorn (2004) in their study of normal faults in Iceland. We tackle normal faults of the Koae fault system, located between the east rift and southwest rift of Kilauea volcano, Hawaii (Fig. 1a). These faults are active, exposures along them are superb (e.g. Peacock and Parfitt, 2002), and structural details of the faulting process are beautifully preserved, making them well suited for our two-pronged approach. To help test how the Koae faults have propagated, we mapped the eastern half of one fault with an 800-m-long scarp. We use field observations of this fault and other larger faults in the Koae system with similar characteristics together with two-dimensional numerical models of faulting in a cross-section perpendicular to fault strike to test whether the faults nucleated at the surface and propagated down, or propagated up from depth.

We begin by presenting our key field observations of surface deformation that bear on fault propagation. We develop a mechanical model to account for the observations, starting with a simple model and then modifying it in stages to better account for our key observations. We conclude by tying the observations and analyses together and presenting a general two-dimensional model for the propagation of normal faults up to the surface in basalt.

2. Overview of the Koae faults

The active normal faults of the Koae fault system occur ~5 km south of Kilauea caldera, between Kilauea's Southwest and East Rift Zones (Fig. 1a). The Koae faults strike east–northeast, roughly parallel to the east rift, and oblique to the southwest rift. The fault system is ~20 km long and 2.5 km wide (Wolfe and Morris, 1996). Fault scarps in the system generally face north–northwest, and they reach heights of ~20 m (Duffield, 1975). Wolfe and Morris (1996) report an age of 400–750 years for most lavas at the surface, yielding average vertical separation rates no less than ~0.03 m/yr at the largest scarps. In the eastern portion of the Koae system, the north side dropped at a rate of 0.03–0.08 m/yr relative to the south side between 1984 and 1991; some faults have slipped continuously since at least 1970 (Delaney et al., 1993). Seismicity and surface fracturing along the Koae faults accompanied deflation of Kilauea's summit in 1938, 1950, 1962, 1965, and 1975 (Fiske and Koyanagi, 1968; Kinoshita, 1968; Lipman et al., 1985). The resolution of seismic data from these earthquakes is not sufficient to meaningfully constrain the depth of the Koae faults or their dip at depth. Our focus is on how the faults propagate; their origin and role in the dynamics of Kilauea volcano are matters of debate and are outside the scope of this paper.

Pioneering work by Macdonald (1957) and Duffield (1975) illuminates key aspects of how the Koae faults have propagated. Macdonald noted that paleo-flow directions in Koae lavas are in many places now oriented either diagonally across or directly up Koae fault scarps. Where we have observed these features we saw no evidence of the associated lava

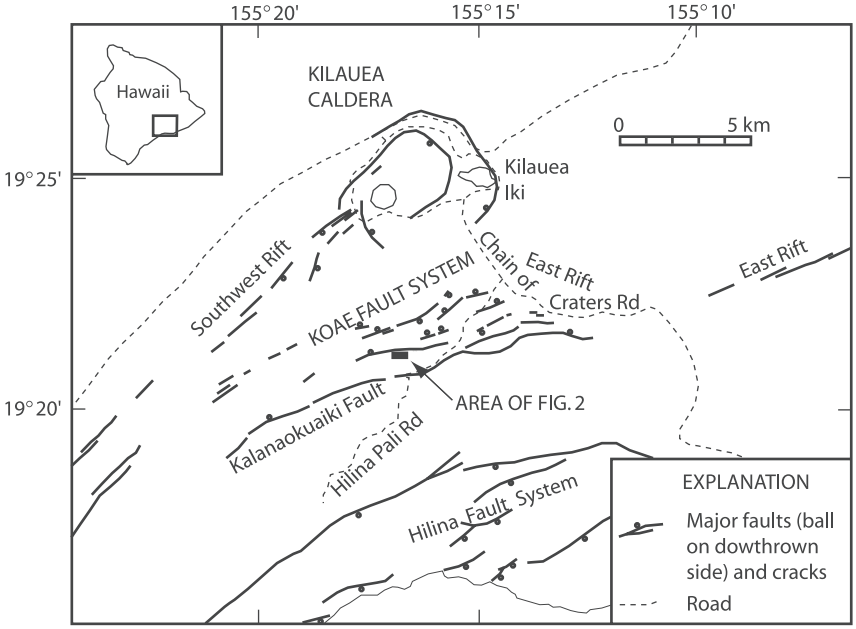

Fig. 1. Map showing the location of the study area (Fig. 2) within the Koae fault system on the south flank of Kilauea volcano, Hawaii.

ponding below the scarp as might be expected if the lava flowed against a pre-existing scarp. This indicates that the current scarps formed after the flows cooled. Macdonald likewise concluded "the monoclines cannot be the result of mantling of fault scarps by flows. Unquestionably they were developed in the thin-bedded lavas after consolidation of the flows." Macdonald observed systematic fractures on the footwall of the monoclines along the scarps, with buckles on the hanging walls. He also noted that the monoclinal flexing was accompanied by opening and closing of vertical joints and by slip between flow layers. Duffield (1975) mapped almost the entire fault system at a scale of 1:7500. He inferred that the fault scarps developed in four general stages. First, échelon cracks opened. Second, the surface warped into a fractured monoclinal flexure. Third, the échelon fractures joined to create gaping fissures, with tilted slabs caught between the échelon segments. Fourth, the tilted slabs collapsed, leaving a steep scarp with rubble at its base. We augment the observations of Macdonald (1957) and Duffield (1975) with new quantitative descriptions and mechanical analyses to provide more insight into the fault propagation process.

3. Field observations of the Ohale fault

The Ohale fault lies between two longer faults near the southern margin of the Koae fault system (Fig. 1). The Kalanaokuaiki fault has the longest trace (~15 km), the tallest scarp (~20 m), and forms the southern boundary of the system (Duffield, 1975). The trace of the Kalanaokuaiki fault is ~0.75 km south of the Ohale fault trace. About 0.2 km north of the Ohale fault is an un-named fault with a trace length of several kilometers and a scarp with an estimated maximum height of 18 m (Duffield, 1975). The Ohale fault scarp faces south–southeast, whereas the scarps of the two neighboring faults face north–northwest. The Ohale fault (Fig. 2) extends ~2 km west–southwest from the Ohale benchmark, with a prominent scarp existing over the easternmost 800 m or so. Its scarp faces are no taller than 3 m, and the maximum throw (i.e. vertical separation) across the fault at the surface is a bit less than 10 m.

We mapped the eastern half of the Ohale fault (Fig. 2) at a scale of 1:1500 using an electronic distance meter, a tape, and a compass. We focus on this part of the Ohale fault for two reasons. It displays some of the best-preserved evidence of how a scarp initially develops, and its features are reflected in faults throughout the Koae system, regardless of the dip direction of the fault.

Surficial lavas along the Ohale fault and in the Koae region, in general, are mainly hummocky pahoehoe flows that dip gently to the south. Local pahoehoe flows are as thick as 2 m, with vesicular zones in the centers of the thickest flows. Volcanic tumuli generally less than 4 m tall punctuate the lava field. Deposits of sediment or ash are generally absent and only locally are more than a meter thick. The minor amounts of sediment, the sparse vegetation, and the freshness of the faulted rocks allow both fine and course structures associated with fault propagation in bedrock to be observed.

3.1. The Ohale fault trace

The Ohale fault, like others in the Koae fault system, has a segmented échelon structure (Fig. 2). Its overall strike is ~N70°E, but the échelon fissures and scarp segments along its eastern portion generally strike east–west and step to the left. The central portion of the Ohale fault trace displays four characteristic features: (1) monoclines locally breached by faults; (2) localized buckles along the scarp base; (3) hanging wall fissures with maximum apertures of a few tens of centimeters; and (4) an échelon array of gaping fissures on the footwall block. Topographic ramps (i.e. 'relay ramps'; Peacock and Parfitt, 2002) occur between échelon scarp segments. Scarp faces reach their maximum height of ~3 m along the central portion of the fault trace. Closer to the fault end, scarps grade into gentle, fractured monoclines, and fissures become less abundant. Past the east end of the fault trace, a monocline is no longer evident, and échelon fissures are sparse.

3.2. Fault scarp profiles

Four profiles across the fault scarp (Figs. 2 and 3) document gross changes in scarp height and morphology from the scarp trace center (A–A′) to the east end (D–D′). Except for profile B–B′, the profiles do not cross large tumuli, so the profiles essentially reflect the effects of faulting and not flow features of the lava field. Accumulations of fault scarp rubble are minor along the profiles and do not complicate estimates of vertical separation across the fault. The profiles have a vertical exaggeration of about three.

Profiles A–A′, B–B′, and C–C′, which are more than 100 m from the fault trace end, have several features in common (Fig. 3a–c). Vertical separation of the lava surface in these profiles is from 6 to 9 m. Each profile is faceted and reveals a footwall surface that is flexed down towards the fault trace. Profiles A–A′ and B–B′ show that the hanging wall surface is flexed down towards the scarp too, providing a shallow basin for the accumulation of sediment and ash, whereas the hanging wall surface on profile C–C′ slopes up slightly towards the scarp. The downward (convex) flexure appears more representative of the central portions of the Koae faults. Profile A–A′ traverses a fractured monoclinal 'bridge' (Fig. 4a) bounded on the east and west by scarps, whereas profiles B–B′ and C–C′ traverse faulted monoclines with scarps of rubble. The vertical separation of the surface across the fault is approximately three times greater than the scarp face height, so the scarp height is a poor measure of the vertical separation of the ground surface across the fault. Fissures are substantially more prominent on the footwall than on the hanging wall. Breaks in slope along the profile of the footwall largely coincide with locations of fissures. The profiles collectively show a monocline along the central portion of the fault scarp, with the monocline being locally breached.

Profile D–D′ (Fig. 3d) differs markedly from the other three profiles. It shows no obvious surface flexure or scarp. Fissures at the north end of profile D–D′ (150–170 m) are not part of the Ohale fault, but rather a fault system north of

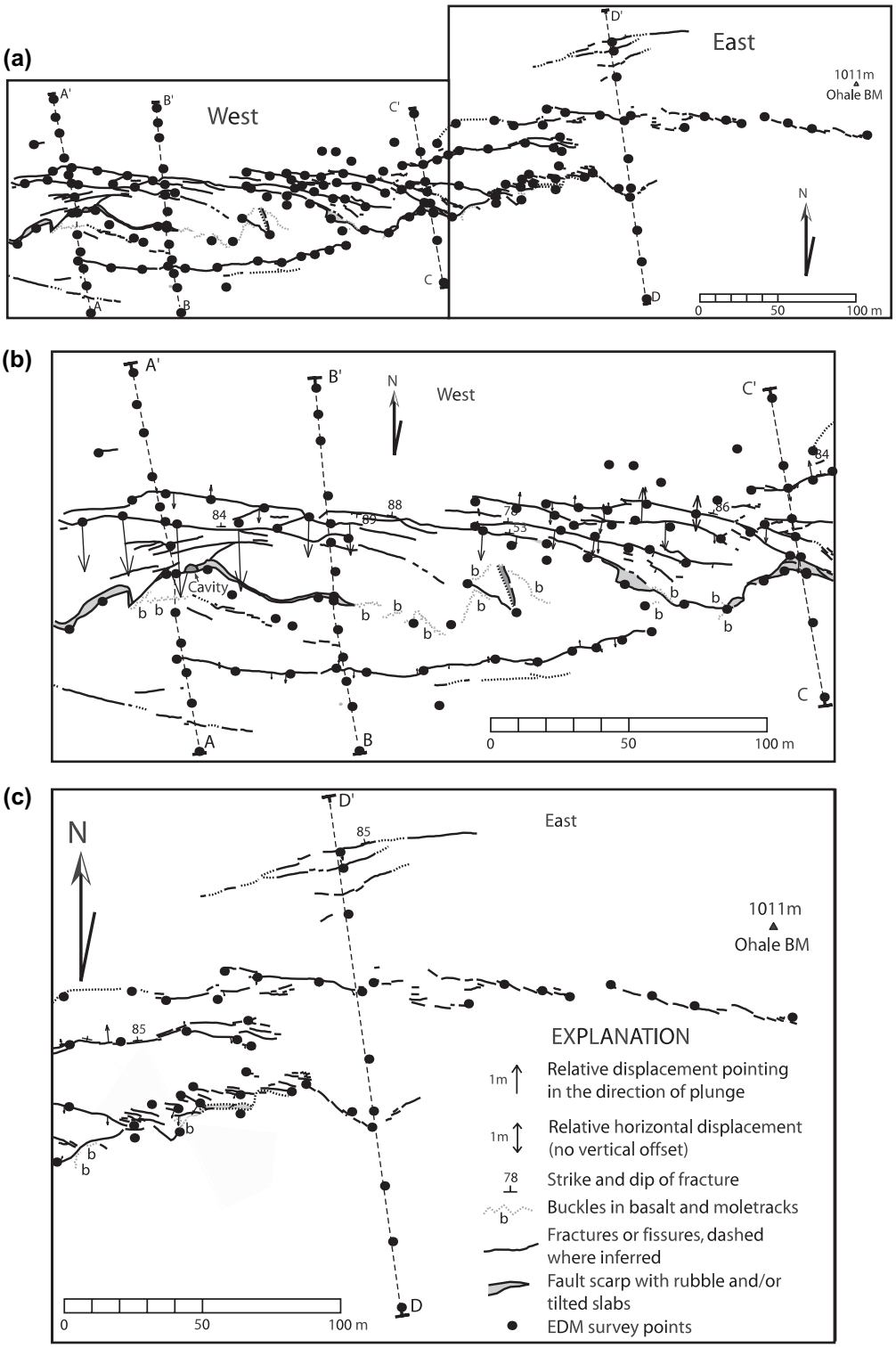

Fig. 2. Map of faults and fissures along the east end of the Ohale fault. (a) Overall map, showing the locations of faults and fissures (solid lines), profile locations (dashed lines), and control points (dots). (b) Western portion of (a). (c) Eastern portion of (a). The explanation of symbols in (c) also applies to (b). The NAD27 coordinates of the Ohale benchmark are19°21′14″ N, 155°16′45″ W. The WGS84/NAD83 coordinates of the Ohale benchmark are19°21′03″ N, 155°16′35″ W.

it (Fig. 2). The single fissure near the center of the profile (~115 m) appears to be a weak continuation of the left-stepping footwall fissure system of the other profiles. The footwall fissuring and relative displacement of the surface across the fault thus diminish towards the fault trace end.

3.3. Monoclines and cavities

Monoclines occur along the fault trace. The central limbs of the monoclines commonly dip ~30–45° to the south. Near profile A–A′ of Fig. 2, a monoclinal bridge is adjacent to

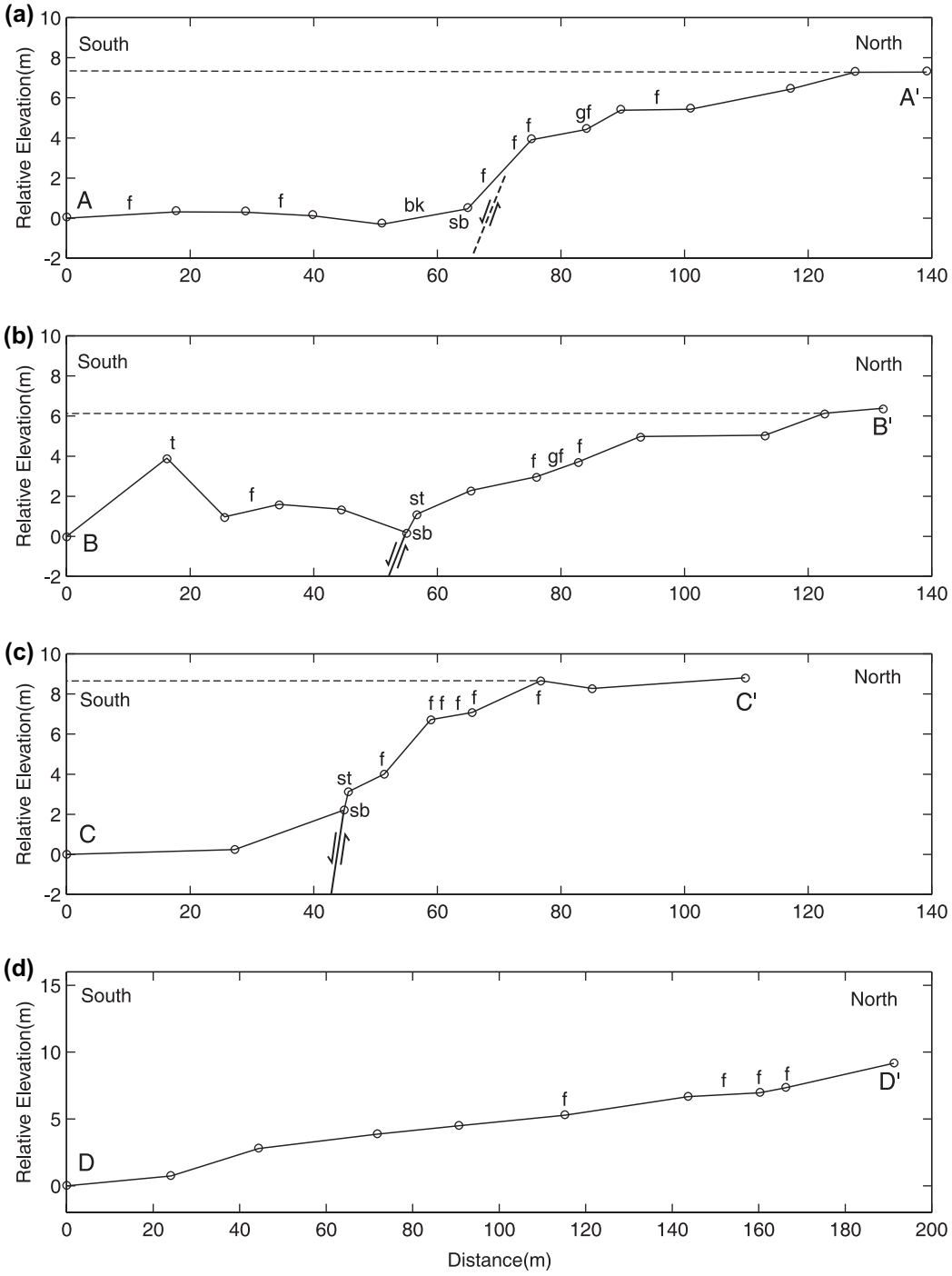

Fig. 3. Topographic profiles across the fault trace; see Fig. 2 for their locations. Circles mark control points. Profile (a) is the westernmost, and profile (d) is the easternmost. The dashed lines serve as references for measuring the relative displacement at the ground surface. Designations on the cross-sections: (f) fissures; (gf) gaping fissures; (t) tumuli; (bk) buckles; (sb) scarp base; and (st) scarp top. The vertical exaggeration is ~3:1, so the inferred fault dip is exaggerated. Note that profile D–D′ is ~60 m longer than the other three.

a nearly vertical scarp (Fig. 4a). This bridge is ~1 m thick and 10 m long. Beneath this bridge is an impressive cavity at least several meters long, a few meters wide, and with a maximum headroom of ~2 m. The cavity is elongate subparallel to the fault trace, is inclined antithetic to the monoclinal slope, and extends down across the lava layers. Blocks that partially fill the cavity separated from their roof along vertical cooling cracks, bedding planes, and vesicle rich zones in the lava flow centers. Cavities like this occur elsewhere beneath monoclines of the Koae fault system, but as best we know they have not been previously documented along fault scarps in the technical literature. The inclination of the cavity across volcanic layering and the presence of nearby flow features indicating paleo-flow directions nearly normal to the fault trace show

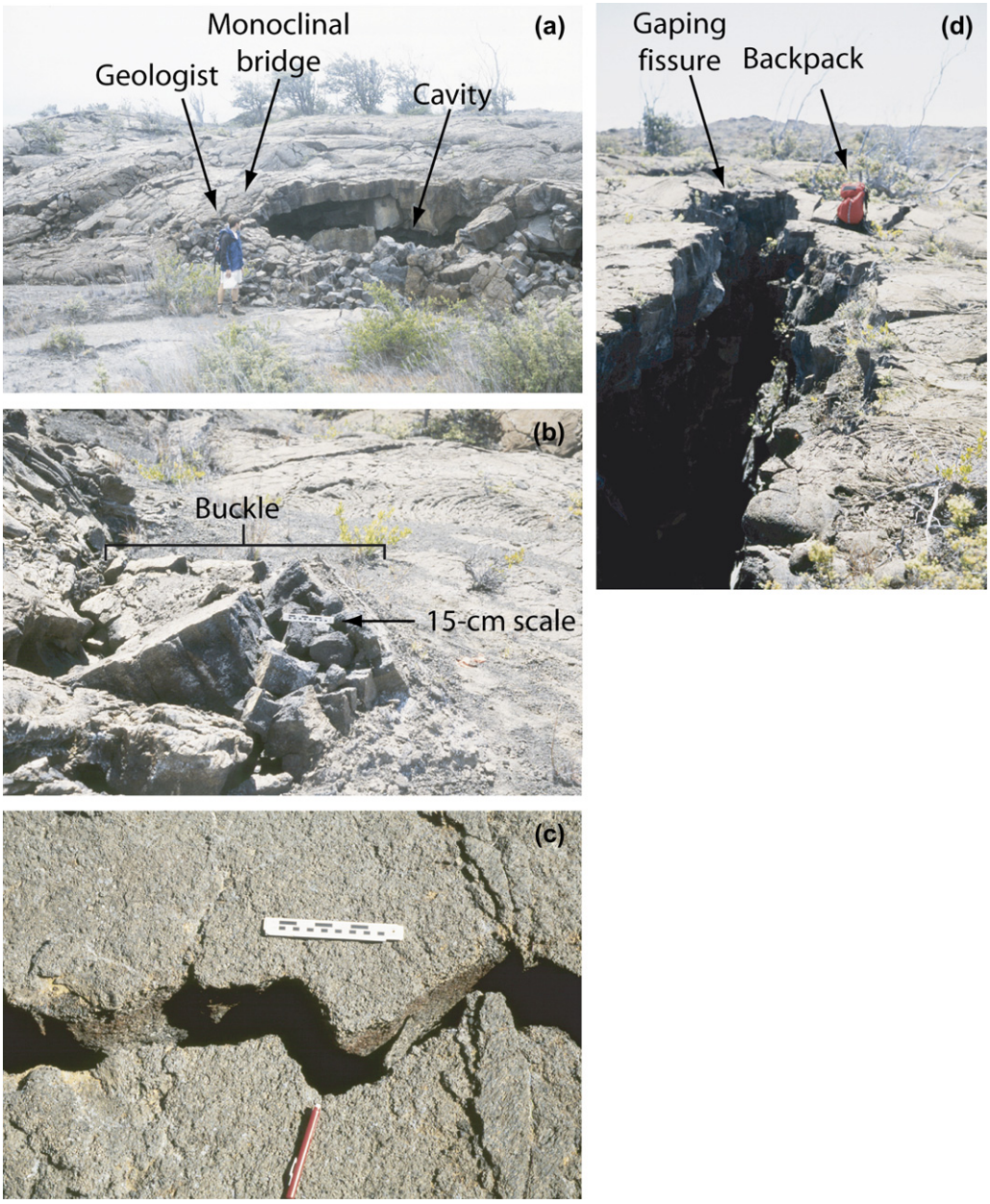

Fig. 4. Characteristic fault structures along the Ohale fault. (a) Monoclinal bridge (at left) with cavity (at right); profile A–A′ crosses the monoclinal bridge behind the geologist. (b) Buckle at base of fault scarp, with 15 cm scale on the buckle. (c) Narrow fissure with jagged edge and 15 cm scale. (d) Gaping footwall fissure, with a backpack for scale to the right of the fissure.

that this cavity is not a lava tube formed by flow parallel to the fault trace. The scarp in Fig. 4a formed by partial collapse of a monoclinal bridge into the underlying cavity.

3.4. Hanging wall buckles

At the scarp base the lava surface is buckled in many places into a sharp anticlinal fold with a fractured crest (Figs. 2 and 4b). The fold axis most commonly parallels the scarp base, but in some places the fold axis is perpendicular to the scarp base. Along the Ohale fault these hanging wall buckles are typically no more than 1 m high, have traces as long as 20 m, and extend across multiple lava flows. Some buckles occur in sediment overlying the basalt; these buckles are referred to as 'moletracks'. The lava flow patterns along the Ohale fault indicate that the scarp is younger than the flows, so the buckles cannot be caused by lava flowing against a scarp (see Section 2). Buckles a few meters tall occur along taller scarps of the Koae fault system. We interpret the buckles as reflecting substantial local horizontal compressive stresses perpendicular to, and locally parallel to, the scarp base.

3.5. Hanging wall fissures

Hanging wall fissures systematically occur near the bases of fault scarps in the Koae system. Where these fissures and

buckles both occur, the buckles are closer to the scarp base. The aperture of hanging wall fissures typically increases with the height of the fault scarp.

Along the Ohale fault, essentially vertical fissures occur 20–50 m from the scarp base on the hanging wall (Fig. 2). These fissures strike subparallel to the fault scarp. They converge towards the east end of the scarp but do not extend all the way to it. The opening direction is approximately normal to the strike of the fissures. In the area of Fig. 2, the maximum cumulative opening across these fissures is a few tens of centimeters. Profiles A–A′ and B–B′ show that the ground surface is convex where intersected by the fissures.

3.6. Footwall fissures

Échelon footwall fissures are perhaps the most spectacular characteristic of the Ohale fault (Fig. 2; see also Duffield, 1975). Pre-existing cooling cracks in the basalts control the detailed trace geometry of fissures, giving them a zigzag appearance (Fig. 4c). They are markedly more abundant on the footwall than on the hanging wall, and they also are much wider. Some have apertures exceeding 2 m; we refer to them as 'gaping' fissures (Fig. 4d). The footwall fissures typically occur 20–30 m from the scarp base, and only where scarp face is more than 1 m high. The gaping fissures are at least 20 m deep. Angular blocks collapsed from the fissure walls choke the gaping fissures and prevent a direct measurement of their true depth. The gaping fissures dip between 84 and 90°. The fissures are roughly perpendicular to the ground surface of the footwall, which now slopes to the south at 3–10° in the vicinity of the fissures, so northerly dips are more common than southerly dips (Fig. 2). The fissures on Fig. 2 generally step to the left and vary in trace length from a few centimeters to more than 100 m. Overall, the fissure traces are linear or curved, with the concave side facing the fault scarp (Fig. 2). Long fissures appear to have formed through linkage of smaller fissures, with linkage locations marked by abrupt jogs and by fractures oblique to the main fissure trend. Tips of unlinked fissure segments generally curve toward, or remain parallel to, a neighboring tip.

The jagged walls allow points on opposing fissure walls to be matched precisely with their original neighbors (e.g. Fig. 4c). The relative displacement across the fissures is primarily opening mode, but small amounts of strike-slip and dip-slip do occur. Two attributes of the fracture walls demonstrate that opening preceded or accompanied slip: (1) the walls lack striations that would indicate the fissure walls slipped while being in contact; and (2) the walls retain irregularities that would have been broken if slip preceded opening. In some places the geometry of the walls required that opening and subsequent lateral slip preceded a partial closure.

We measured the relative displacements across the fissures at about 100 spots, shown with arrows on Fig. 2. Arrows point from the uplifted piercing points to the corresponding down-dropped partners. Double arrowheads show spots with no detected relative vertical displacement. The measurements, made with a tape, compass, and Abney level, have errors of less than a centimeter. The mean strike of individual fissures is 275° (Fig. 5a). The mean horizontal component of relative displacement is nearly due north–south (Fig. 5b). About 91% of the relative horizontal motion across individual fissures then is due to opening, and ~9% is due to left-lateral slip.

Fig. 6 shows a relative displacement profile along the fissure system within the mapped area (Fig. 6). A smooth interpolation function fits data points along each fissure to construct individual relative displacement profiles. Dip-slip

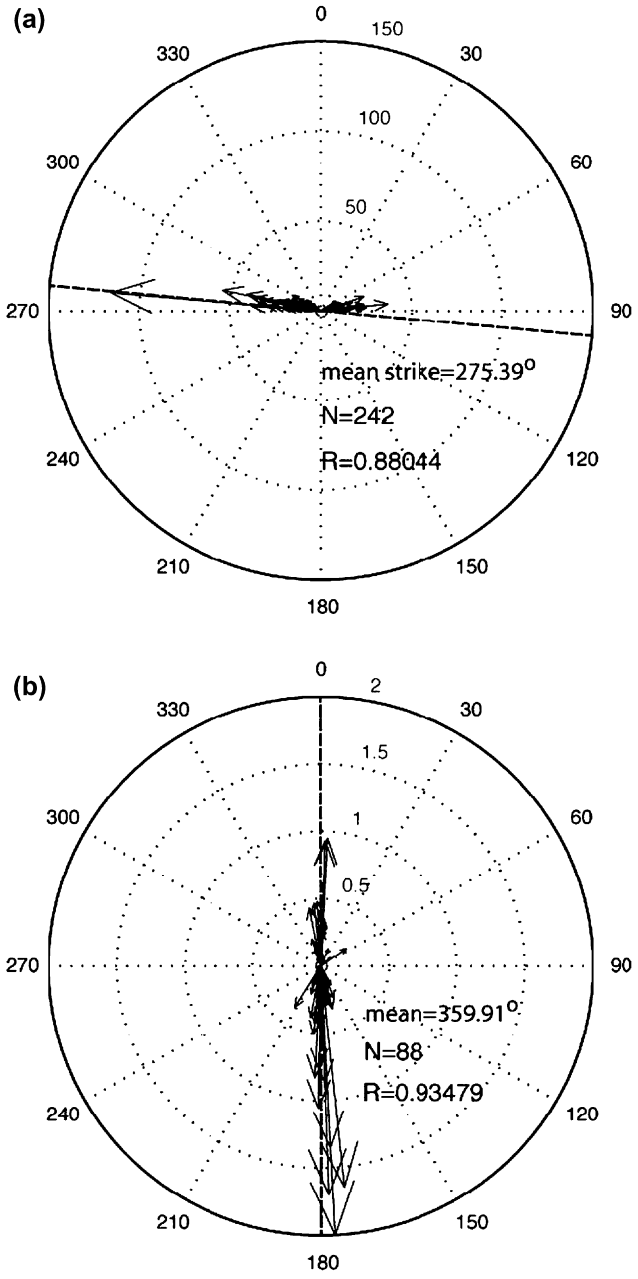

Fig. 5. Compass plots of (a) strikes of fissures in Fig. 2, and (b) the horizontal component of relative displacements across the fissures. Weighted mean orientations are shown as dashed lines (the weighting factor is the fissure length). Plot radii are fissure length in (a) and relative displacement vector length, in m, in (b). The number of measurements is N, and R is the length of the weighted mean resultant in meters.

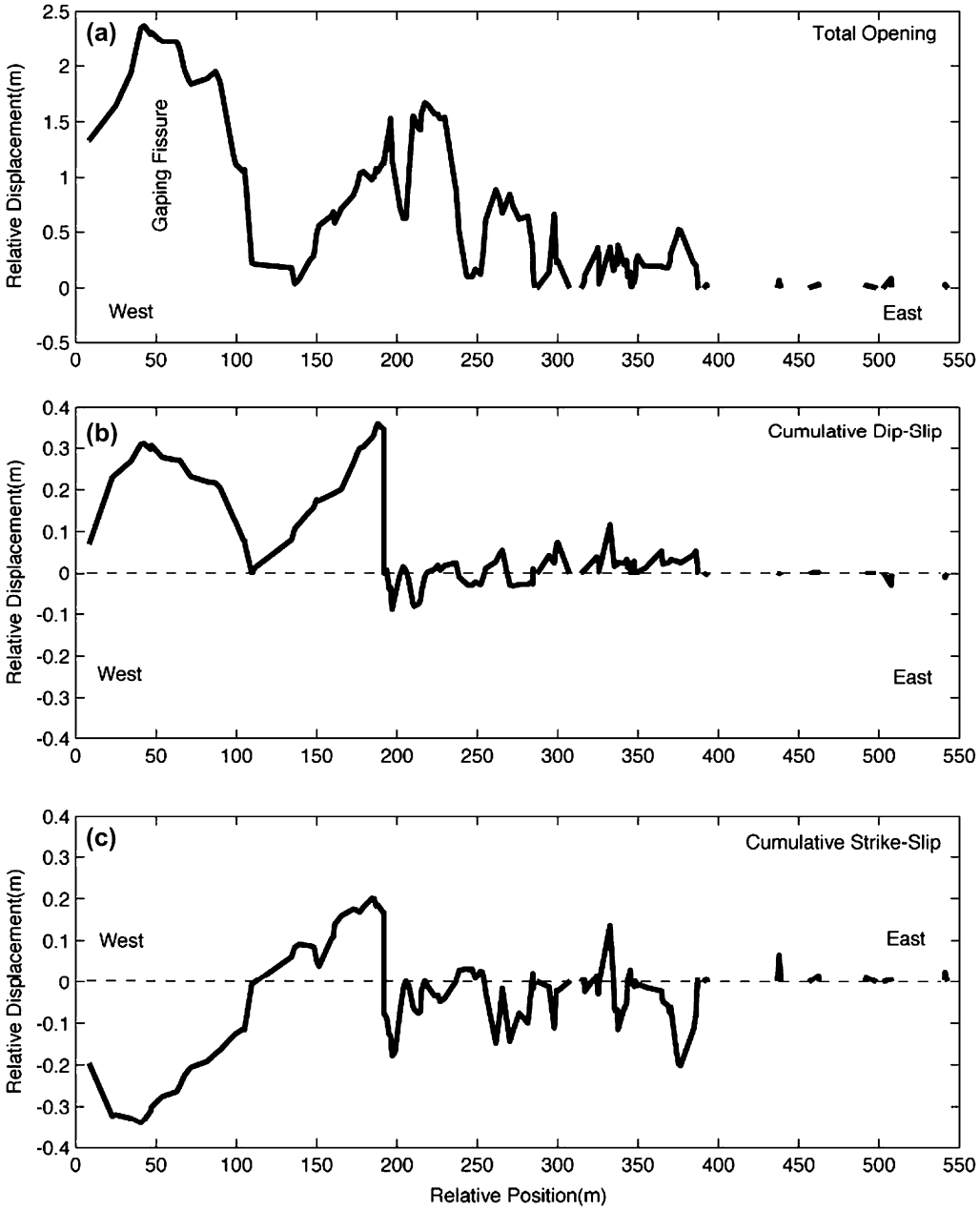

Fig. 6. Components of cumulative relative displacement across measured fissures in Fig. 2. (a) Total opening, (b) cumulative dip-slip, and (c) cumulative strike-slip relative displacement. Each component is projected onto a vertical plane parallel to the mean fracture strike (Fig. 5a). Positive dip-slip and positive strike-slip represent north side up and right lateral shear, respectively.

and strike-slip components are obtained by projecting the relative-displacement vector data onto a vertical plane striking 275°; opening components are derived from projecting the data normal to the mean strike plane. Data from overlapping fissures are summed to create the cumulative distribution. Gaps in the curves reflect the absence of measurements. Measurements of fissures at the north end of profile D–D′ are left out of the cumulative calculations because those fissures link to another fault trace north of the Ohale fault (Figs. 1 and 2). Fig. 6 reveals that the opening components are about an order of magnitude greater than the strike-slip and dip-slip components. Opening tapers irregularly towards the east end of the fault (Fig. 6a). Maximum amounts of opening coincide with gaping fissures, and opening decreases as the relative abundance of fissures decreases. The dip-slip component (Fig. 6b) is ~10% of the opening component. The south side is usually down, the same as the fault (e.g. see the gaping fissure at ~50 m on Fig. 6). The strike-slip profile (Fig. 6c) shows a small left-lateral component along most of the fissures, consistent with Fig. 5. In contrast, the north–south mean opening direction yields a right-lateral component of slip relative to the N70°E trace of the fissure system as a whole; this is consistent with the general left-stepping pattern of fissures at the east end of the fault.

4. Mechanical analysis

To understand the origin and formation of the monoclines, cavities, buckles, hanging wall fissures, and footwall fissures that accompany normal fault propagation we conducted a series of two-dimensional analyses of faulting in a cross-section perpendicular to fault strike. Our analyses first address an isolated fault, treating conditions at the surface and at depth. Next we consider the interaction of a fault and a footwall fissure, and then the interaction of a primary fault with a smaller antithetic fault. This section concludes with an analysis of the factors affecting the displacements at the ground surface. Three-dimensional issues such as the effect of fault tip-line shape, the interaction between fault segments along strike, and the échelon nature of the fissures along fault strike are outside the scope of this paper.

4.1. Solution method, boundary conditions, and model parameters

For our analyses we employed a half-space version of the plane strain displacement discontinuity code TWODD (Crouch and Starfield, 1983). This code is widely used to calculate stresses and displacement in bodies with fractures and faults (e.g. Lin and Parmentier, 1988; Olson and Pollard, 1989; Bruhn and Schultz, 1996; Martel, 2000; Martel and Muller, 2000). We treat the host rock here as a linear elastic, isotropic, isothermal, homogeneous, semi-infinite continuum. The appendix gives the two functions needed to convert TWODD from an infinite body code to a code for examining a half-space with a traction-free horizontal surface.

We idealize the Ohale fault as planar and fix its lower tip at a constant depth but note that its actual down-dip geometry is not known. A reasonable maximum down-dip extent for the Ohale fault comes from considering the measurements of Nicol et al. (1996). In their study of about 20 'vertically restricted' normal faults in sedimentary rock layers, they found the faults exhibited a ratio of trace length to maximum down-dip extent of 1.8–8.4. We expect volcanic layering would have an effect analogous to sedimentary bedding and use this ratio range. Given the Ohale fault trace length of 2 km, the maximum down-dip extent of the fault would be ~1 km. If the Ohale fault and the much larger Kalanaokuaiki fault to the south dip towards each other at 70°, they would intersect at a down-dip extent of 1.03 km (analyses to come will show that a dip (δ) of 70° is reasonable based on mechanical considerations and field observations).

The plane $y=0$ describes the ground surface prior to faulting, with $y<0$ below the surface. The x-axis is horizontal and normal to fault strike. In most simulations the fault projects to intersect the surface at $x=0$, $y=0$. Points at the surface where $x<0$ are on the hanging wall, and points where $x>0$ are on the footwall.

We model the fault as frictionless, as do Willemse et al. (1996), Cooke and Pollard (1997), and Crider and Pollard (1998). Since our model faults are frictionless and extend an infinite distance along strike, slip across them will exceed the slip across a real fault with the same down-dip extent. The model thus yields a well-defined end-member of possible fault behaviors useful for understanding fault propagation. Unless otherwise noted, we model faults exclusively as shear fractures and require the fault walls to remain in contact during slip. Our results are compatible with this: any opening along the fault that might occur due to faulting-induced stresses would be tiny relative to the slip and highly localized. As we only model planar faults, we do not (and cannot) account for local openings along a fault associated with deviations from planarity (e.g. Ferrill and Morris, 2001).

Defining simple, potentially realistic, and physically admissible ambient (i.e. 'far-field') stresses for the Koae region is problematic. The subaerial and submarine parts of the south flank are free to move seaward (Swanson et al., 1976), whereas the north slope of Kilauea is buttressed by Mauna Loa. The situation is also complicated by nearby normal faults of the Koae and Hilina systems (Fig. 1) and a subhorizontal detachment fault near the base of Kilauea (Owen et al., 1995). We consider a simple range of distributions where the ambient normal stresses vary linearly with depth:

$$\begin{aligned}\sigma_{yy}^{\infty} &= \rho g y \\ \sigma_{xx}^{\infty} &= C\rho g y \\ \sigma_{xy}^{\infty} &= 0\end{aligned} \tag{1}$$

where ρ is the bulk host rock density of 2300 kg/m^3 (Kinoshita et al., 1963), g is acceleration due to gravity (9.8 m/s^2), and y is vertical position ($y<0$), and C is ratio between the ambient horizontal normal stress (σ_{xx}^{∞}) and the ambient vertical normal stress (σ_{yy}^{∞}). In our convention tensile stresses are positive, and negative stresses are compressive. Martel and Muller (2000) and Martel (2000) describe how non-uniform ambient stresses such as these are accounted for using TWODD. The magnitude of the ambient shear stress parallel to the fault is then:

$$\tau^{\infty} = (1-C)\rho g y \sin\delta\cos\delta \tag{2}$$

where δ is the fault dip. Slip on a fault with no shear strength is permitted for $0\leq C<1$ and our results can be used for that full range. A reasonable range for C for Kilauea is 0 to 1/3, where $C=0$ for a laterally unconfined body, and $C=1/3$ for a laterally confined elastic body assuming a Poisson's ratio of 0.25. Measurements from sedimentary basins in the US (McGarr and Gay, 1978) are consistent with values of C between 0.7 and 0.8, close to the theoretical limit of 0.85 for normal faulting, assuming that laboratory values of friction apply (Engelder, 1993). The slip and the stress perturbations induced by slip on our frictionless model fault scale with τ^{∞} and hence with $1-C$. By scaling certain of our plots by $1-C$ we can represent either the faulting-induced displacements or the stress perturbations for a range of ambient stress fields on a single plot. Both τ^{∞} and the fault slip decrease as (a) C increases from zero towards one, and (b) as δ increases from 45 to 90°.

We use a Young's modulus E of 5 GPa to simulate the basalt of the Koae region. This is the value Gudmundsson (2000) favors for the uppermost few hundreds of meters of the rift

zone in Iceland. Rubin and Pollard (1987) estimated that the in situ shear modulus along Kilauea's southwest zone is within a factor of 2–3 of 3 GPa, yielding a corresponding Young's modulus range of 2.5–18.5 GPa assuming a Poisson's ratio of 0.25. Our value lies within this range. It lies at the low end of the range of 5–50 GPa considered to reflect the in situ modulus for a "good quality rock mass that contains numerous weathered joints" (Schultz, 1993). In our two-dimensional model, the internal stresses are independent of E, but the displacements induced by faulting vary inversely with it. For example, if Young's modulus were reduced by 1/3, then the displacements would increase by 50% but the stresses would be unchanged.

4.2. Analysis for the ground surface for an isolated fault

We first examine the horizontal (u_x) and vertical (u_y) displacements, and the horizontal normal stress σ_{xx} stress at the free surface for isolated planar faults with dips of 60 and 70°. The down dip extent of the lower tips of the faults in these analyses is 1.03 km.

Fig. 7 shows the horizontal displacements, vertical displacements, and horizontal stress normal to the fault strike at the surface for an isolated fault with a dip of 60°. Note that the displacements increase sharply once the fault breaks the surface. The vertical displacements (Fig. 7b) show that for a 'blind' fault tip below the ground surface, the model produces a monoclinal flexure, and the maximum slope on the monocline increases as the upper fault tip approaches the surface. The peak horizontal tensile stress lies close to x=0. Other test results, not shown here, reveal that as the fault dip decreases below 60° the peak horizontal tensile stress lies on the hanging wall. The most pronounced fissures for fault dips of 60° or less would tend to open on the hanging wall rather than the footwall, contrary to field observations. A fault dip less than 60° is therefore unlikely to account for the field observations.

Fig. 8 shows results for an isolated fault with a dip of 70°. The displacements are slightly less than for the case of a 60° dip (Fig. 7) owing to the lower ambient fault-parallel shear stress (Eq. (2)). Again, the vertical displacements (Fig. 8b) reveal a monocline if the upper tip of the fault is below the surface. For a surface-breaking model fault, the monocline disappears, the hanging wall surface becomes relatively planar and dips toward the fault trace, and the footwall surface dips away from the fault trace. Of the hanging wall profiles in Fig. 3, only A–A′, which has the fewest fissures, resembles the model prediction for a surface-breaking fault. We infer that the key discrepancies between the profile shapes on the footwall of the Ohale fault (Fig. 3) and the model profile shape for surface-breaking faults in Fig. 8 are largely because our model for Fig. 8 has no fissures on the footwall and does not account for irrecoverable, non-elastic deformation, including fracturing and bedding plane slip. The modeled throw

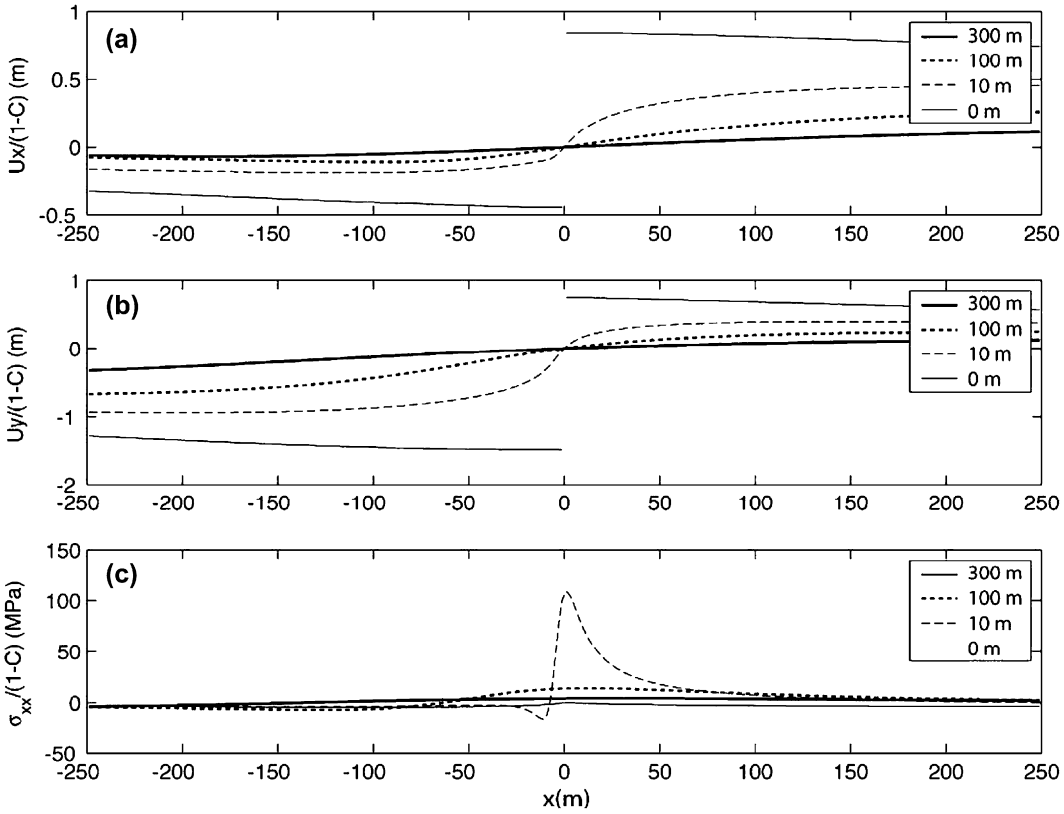

Fig. 7. Model displacements and stresses at the surface for a normal fault dipping 60°, with the upper tip at various distances down dip from the surface: 300, 100, 10, and 0 m. (a) Horizontal displacement. (b) Vertical displacement. (c) Horizontal stress perpendicular to fault strike (tension is positive). See Section 4.1 for a description of the parameter C.

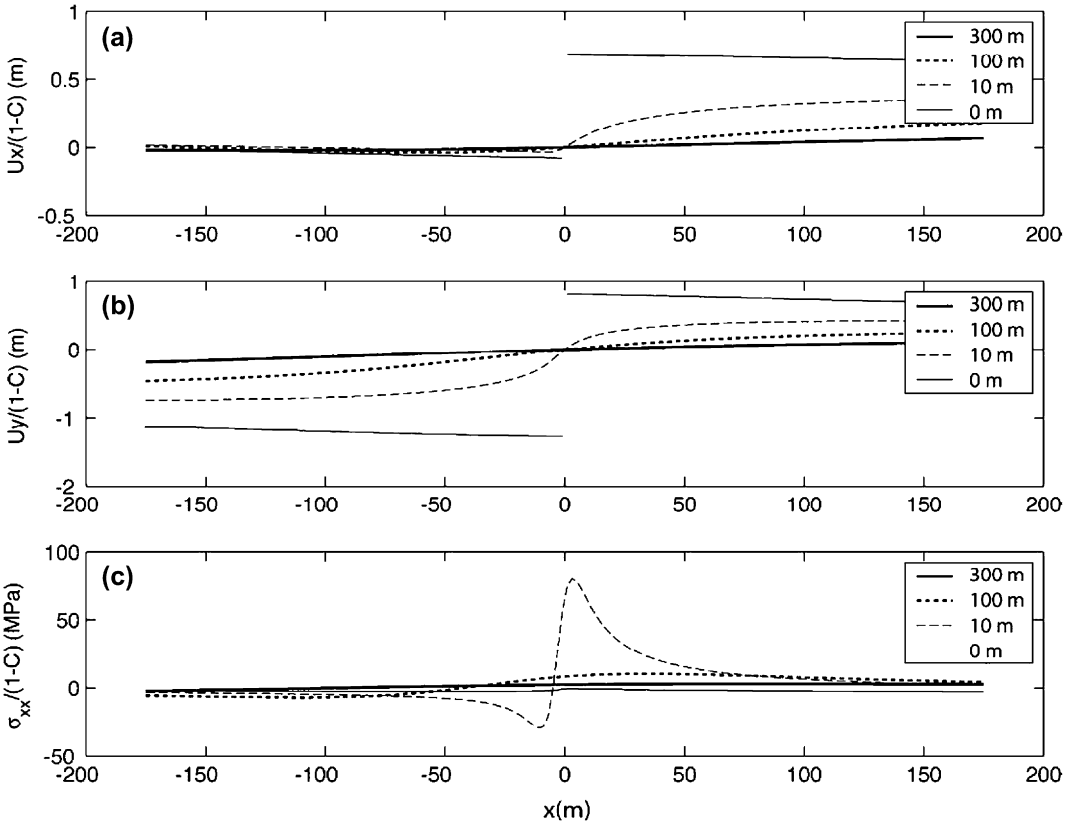

Fig. 8. Model displacements and stresses at the surface for a normal fault dipping 70°, with the upper tip at various distances down dip from the surface. (a) Horizontal displacement. (b) Vertical displacement. (c) Horizontal stress perpendicular to fault strike (tension is positive).

across the fault is ~1/3 of what is observed, a point we will return to subsequently.

The horizontal stress (Fig. 8c) shows peaks of tensile and compressive stress on the footwall and hanging wall, respectively, as the fault approaches the surface. These results are consistent with the presence of pronounced fissures on the footwall and buckles on the hanging wall. The tensile and compressive stress peaks shift towards x=0 m and become more pronounced as the fault tip approaches the surface. This suggests that footwall fissures open progressively closer towards a fault scarp as a scarp develops, and that the buckles at the base of the scarp form as the fault tip nears the surface. The peak horizontal tensile stress in Fig. 8c is ~90 MPa for a fault tip depth of 10 m and C=0, well above the stress of 18 MPa required to propagate a pre-existing cooling fracture a millimeter long through basalt with a fracture toughness of ~1 MPa/m$^{1/2}$ (Atkinson and Meredith, 1987). The peak compressive stress on the hanging wall is ~30 MPa (at $x \approx -10$ m) for a fault tip depth of 10 m. To see if these stresses are great enough to cause buckling, we solve for the minimum force per unit plate breadth (P_c) required for buckling a thin, linear elastic plate (Turcotte and Schubert, 1982, eqs. 3-73 and 3-95):

$$P_c = \frac{\pi^2 E h^3}{12 L^2 (1-\nu^2)} \quad (3)$$

The length (L) and thickness (h) of the plate are set to 3 m and 0.3 m, respectively (see Fig. 4b). A plate 1 m deep with these parameters would require approximately 13 MN to buckle. Dividing the buckling force by the cross-sectional area of the plate end yields the minimum buckling stress (σ_b):

$$\sigma_b = \frac{13\ \text{MN}}{0.3\ \text{m}^2} \cong 43\ \text{MPa} \quad (4)$$

The calculated compressive stress of 30 MPa is about 30% less than 43 MPa. For the model parameters used, the fault tip would need to be close to the surface (within ~10 m) to cause buckles like those observed along the Ohale fault. In our two-dimensional analysis the compressive stress parallel to the fault strike will also be increased, albeit not as much as perpendicular to the fault trace. Local conditions might allow for buckles with axes that are not just parallel to the fault trace, and some of these are observed (Fig. 2). The modeling results also indicate that footwall fissures are likely to form before hanging wall buckles. This is consistent with two observations: (a) footwall fissures occur on monoclines whether or not buckles are present, and (b) buckles only occur where fissures are present.

The model results for a fault growing toward the surface are qualitatively consistent with three recurring surface relations along the Ohale fault and other Koae faults: monoclines along the fault traces; fissures on the footwalls, and buckles on the

hanging walls. Two lines of evidence indicate that these characteristics are not accounted for by a two-dimensional fault that grows down from the surface. First, scarps occur for all faults, and no monoclines are produced (Fig. 9b). Second, mild compressive horizontal stresses at the surface are predicted on both sides of the fault near the fault trace (Fig. 9c); this condition would not allow a fissure to open on the footwall and might be inadequate for buckling. We therefore conclude that the faults grew up towards the surface rather than down from it.

4.3. Analysis of the subsurface for an isolated fault

To further address the development of structures along the Ohale fault, we calculate stress fields in the upper 300 m of the subsurface. The effect of fault slip on pre-existing horizontal flow boundaries and on vertical fractures is of interest, so we consider the horizontal stress field (σ_{xx}), vertical stress field (σ_{yy}), and the orientation of the most compressive stress (σ_2). If σ_{xx} or σ_{yy} is tensile, then opening is expected across weak flow boundaries or pre-existing vertical cooling fractures, respectively. If both stresses are tensile, then fractures of all orientations could open. The trajectories of the most compressive stress serve as a proxy for the orientation of cracks that might open.

Fig. 10 shows the horizontal stress field and most compressive stress trajectories for a fault dipping 70°. The ambient horizontal stress field is one of no lateral confinement (C=0).

For a deep blind upper fault tip (Fig. 10a), tensile stresses, shown in gray, prevail on the footwall above the fault tip; they are concentrated at the surface on the footwall and above the fault tip on the hanging wall. This indicates that the footwall fissures would nucleate at the surface and could propagate down to about the level of the upper fault tip. The fissures could extend more than 100 m down from the surface.

As the fault approaches the surface (Fig. 10b and c), the tensile field shrinks in size, but the tensile stress concentrations increase both at the surface and near the fault tip itself, with the tip actually becoming enveloped in a 'tensile stress cloud'. These are effects of the interaction between the fault and the surface, for analogous effects do not occur for a fault in an infinite medium (Pollard and Segall, 1987). For example, the fault of Fig. 10c develops a tension as high as 1.5 MPa across the upper 3 m of the fault tip if $\sigma_{xx}^{\infty} = 0$ (i.e. C=0). This could cause the upper 3 m of the fault tip to open by about a millimeter, about two orders of magnitude less than the slip there (a few decimeters). Such an opening over such a short length of the fault would have a negligible effect on surrounding structures and on fault propagation. As C increases, the slip and the slip-induced tension decrease, whereas the ambient compressive stress across the fault increases, so the opening will be less than a millimeter for C>0. This finding supports our use of a boundary condition

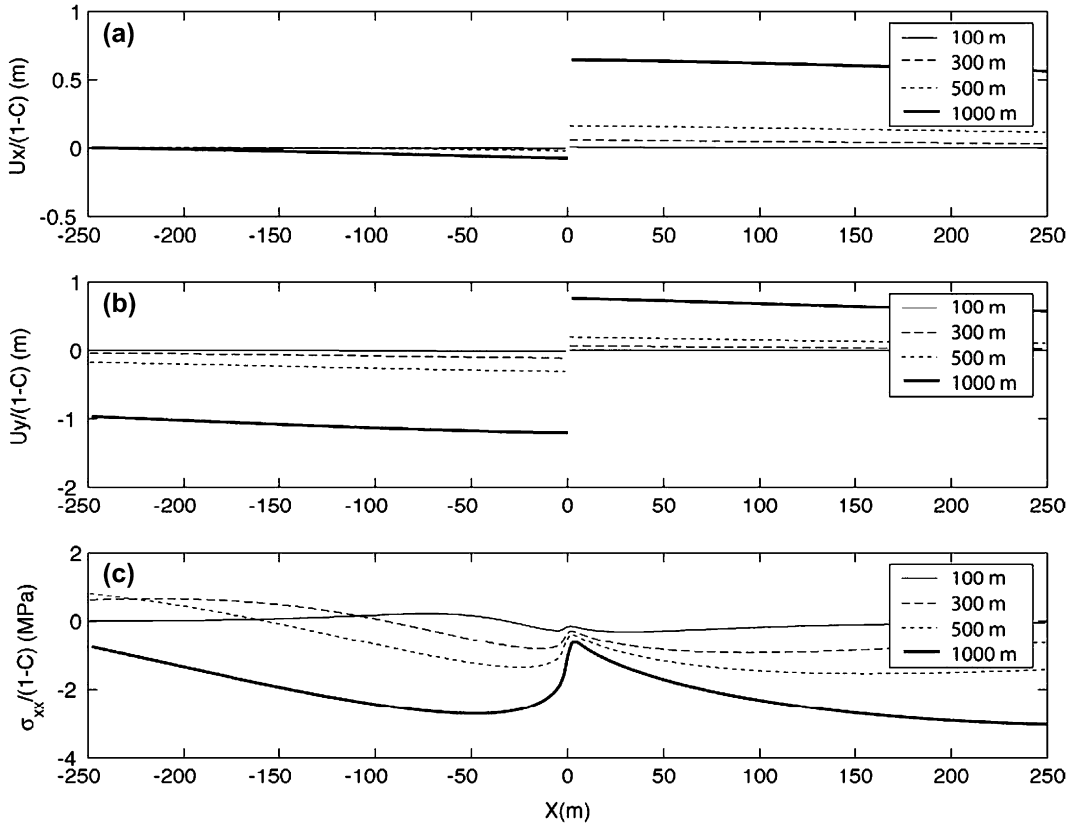

Fig. 9. Model displacements and stresses at the surface for a normal fault dipping 70°, with the upper tip at the surface and the lower tip at various distances down dip from the surface: 300, 100, 10, and 0 m. (a) Horizontal displacement. (b) Vertical displacement. (c) Horizontal stress perpendicular to fault strike (tension is positive).

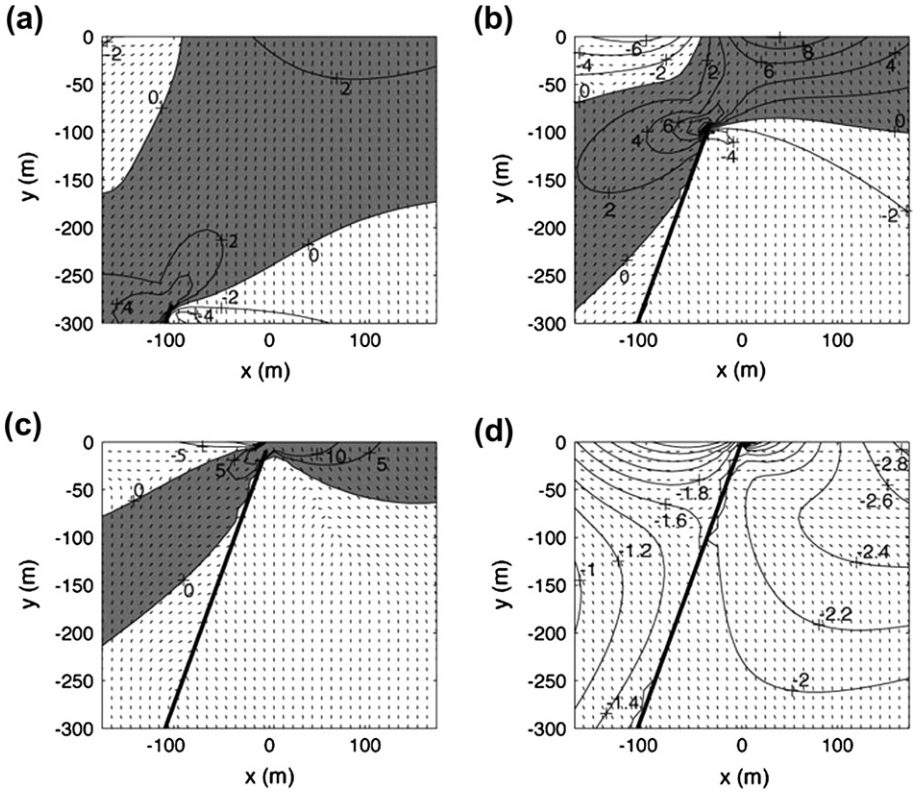

Fig. 10. Cross-sections showing the horizontal stress magnitude for a normal fault dipping 70°, with the upper tip at various distances down-dip from the surface: (a) 300 m; (b) 100 m; (c) 10 m; (d) 0 m. The ambient horizontal stress is zero (i.e. C=0). Tick marks are perpendicular to the direction of greatest tensile stress and show the dips of potential fractures. Regions in gray mark areas of horizontal tension. Regions in white mark areas of horizontal compression.

whereby the fault walls stay in contact in our study of fault propagation.

As the fault approaches the surface (Fig. 10), the compressive stress maximum at the surface shifts along the hanging wall towards x=0 and increases in magnitude reflecting an increased tendency for buckling. Trajectories of σ_2 are nearly vertical in regions of tension on the footwall, horizontal at the top of the hanging wall, and dip 45–90° in the direction of fault dip in the region of tension on the hanging wall. The conditions favor vertical fractures in the footwall, promote horizontal buckling in the hanging wall above the fault tip, and allow normal faulting in the hanging wall near the fault tip. The trajectories of σ_2 at the surface of the footwall are nearly vertical in Fig. 10b but are inclined in Fig. 10c. This means that after footwall fissures open they might subsequently slip as the fault tip propagates towards the surface.

For a fault that breaks the surface (Fig. 10d), the horizontal stresses become compressive. This model prediction is apparently at odds with the presence of open footwall fissures adjacent to faults that break the surface (i.e. scarps). We suggest that the footwall fissures, especially the gaping fissures, remain open due to propping by boulders that have fallen from the fissure walls.

Fig. 11 shows the vertical stress field, which can be used to infer where either horizontal flow boundaries or horizons of vesicles might split. Close to the upper tip of a deep blind fault (Fig. 11a), a tensile stress concentration develops on the hanging wall. A horizontal tensile stress concentration also occurs there (Fig. 10a), so pre-existing cracks of any orientation could open there and create a cavity. As the fault tip approaches the surface (Fig. 11c), so does the region of vertical tension, with a field of weak vertical tension developing near the surface of the footwall. The results thus suggest that the cavities nucleate at depth on the hanging wall, and grow with the fault tip as the tip propagates toward the surface. When the fault tip reaches the surface (Fig. 11d), the vertical stresses become compressive, so in a perfectly elastic material no voids would remain open for a fault that breaches the ground surface. We infer that non-elastic effects, such as fracturing and stoping of blocks from cavity walls, plays a role in keeping the cavities open as well as in helping them to form in the first place.

4.4. Fault and fissure analysis

In light of our previous results, we now examine a fault with a neighboring fissure. The fissure is represented as a vertical traction-free crack at x=+26 m that extends from the ground surface to 150 m depth. In the absence of a fault, the ambient stresses do not permit vertical cracks to open or slip; any relative displacement across the fissure reflects stress perturbations caused by fault slip.

Model displacements at the surface for the fault-fissure system show the fissure both opens and slips (Fig. 12). If the fault

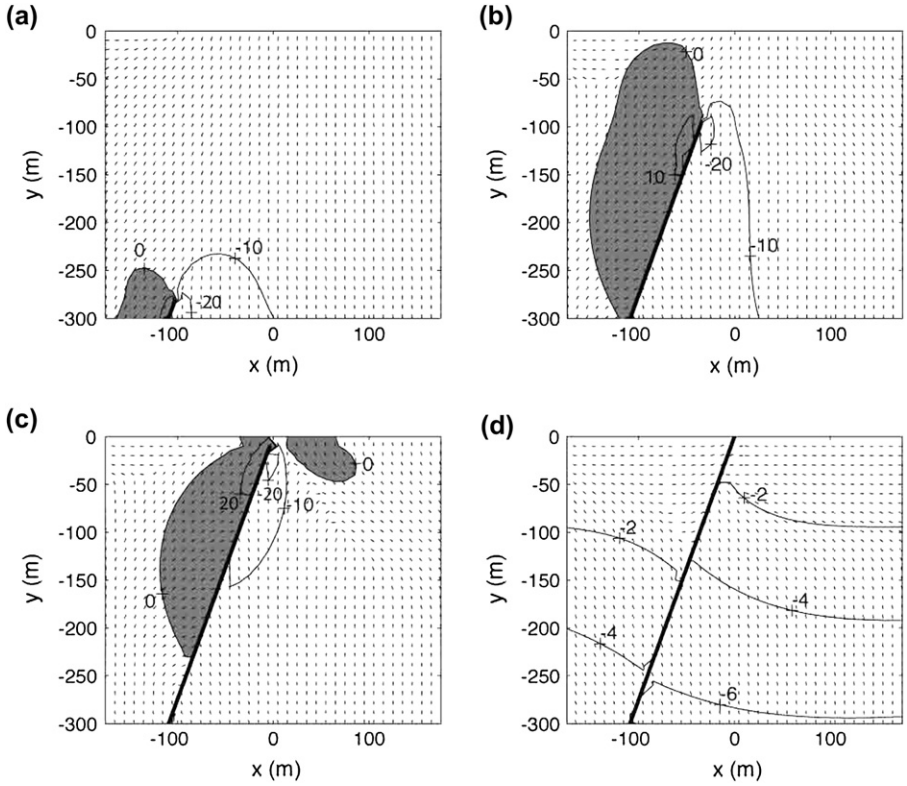

Fig. 11. Cross-sections showing the vertical stress magnitude stress for a normal fault dipping 70° with the upper tip at various distances down dip from the surface: (a) 300 m; (b) 100 m; (c) 10 m; (d) 0 m. The ambient horizontal stress is zero (i.e. C=0). Tick marks are perpendicular to the direction of greatest tensile stress and show the dips of potential fractures. Regions in gray mark areas of vertical tension. Regions in white mark areas of vertical compression.

does not break the surface, then the horizontal displacements at x=+27 m are more positive than those at x=+25 m (Fig. 12a), and the fissure opens. In contrast, if the fault breaks the surface (Fig. 12a, thin solid line), then the model predicts that the fissure walls would interpenetrate. This supports our interpretation that fallen blocks from the fissure walls help prop the fissures open. The predicted dip-slip across the fissure (Fig. 12b) is about an order of magnitude less than the amount of opening. This is consistent with our observations (Fig. 6). The predicted sense of dip-slip across the fissure depends on the fault tip depth. For fault tips at depths of 300 and 100 m, the wall of the fissure near the fault drops down, but the reverse occurs for tips at depths of 10 and 0 m. Both senses of slip are observed, with the former sense of slip occurring primarily on the widest fissures and the reverse on the narrower ones (Figs. 2 and 6). The inability of the fissures to close might explain why the sense of dip-slip generally does not reverse when the fault breaks the surface. For a fault tip at a down-dip depth of 10 m, the predicted fissure opening is ~0.7 m, about 1/3 the maximum amount observed. This is about the same as the ratio of predicted fault throw at the surface to the observed throw. We return to this point shortly. Finally, a comparison of Figs. 8b and 12b shows that the fissure does not materially affect the throw of the fault at the surface.

The footwall fissure also affects σ_{xx} at the surface. For a fault tip at a down-dip depth of 10 m (Fig. 12c), the peak compressive stress on the hanging wall is 44 MPa, ~40% greater than the level if the footwall fissure is absent (Fig. 8c). The opening of the footwall fissures thus contributes to the tendency for buckling at the scarp base. A tensile stress concentration remains on the footwall between the fissure and the fault trace, so the opening of one fissure does not preclude the opening of others. If the fault does break the surface, then a broad but weak horizontal tension is predicted at the surface of the hanging wall (Fig. 12c, thin solid line). This broad tensile stress distribution is unlikely to account for the observed concentration of fissures on the hanging wall.

4.5. Master fault, fissure, and antithetic fault

The analyses presented so far do not account for the fissures on the hanging wall, indicating that our model is incomplete. Observations of the Koae faults show that the hanging wall fissures increase in length and aperture as the fault scarp height increases, suggesting that the fissures form late in the fault growth process. We consider now whether these fissures might be due to antithetic faulting. Our analyses are prompted in part by clay model experiments that show antithetic faults developing on the hanging wall near the tip of a laboratory-scale normal fault as it propagates towards the surface (Withjack et al., 1990).

Fig. 13 shows the displacements and horizontal stresses at the surface for a fault–fissure system with three elements: a blind master fault that dips 70°, with an upper tip 5 m down-dip from the surface; a vertical footwall fissure 150 m deep at x=26 m; and a blind antithetic fault that dips 70°

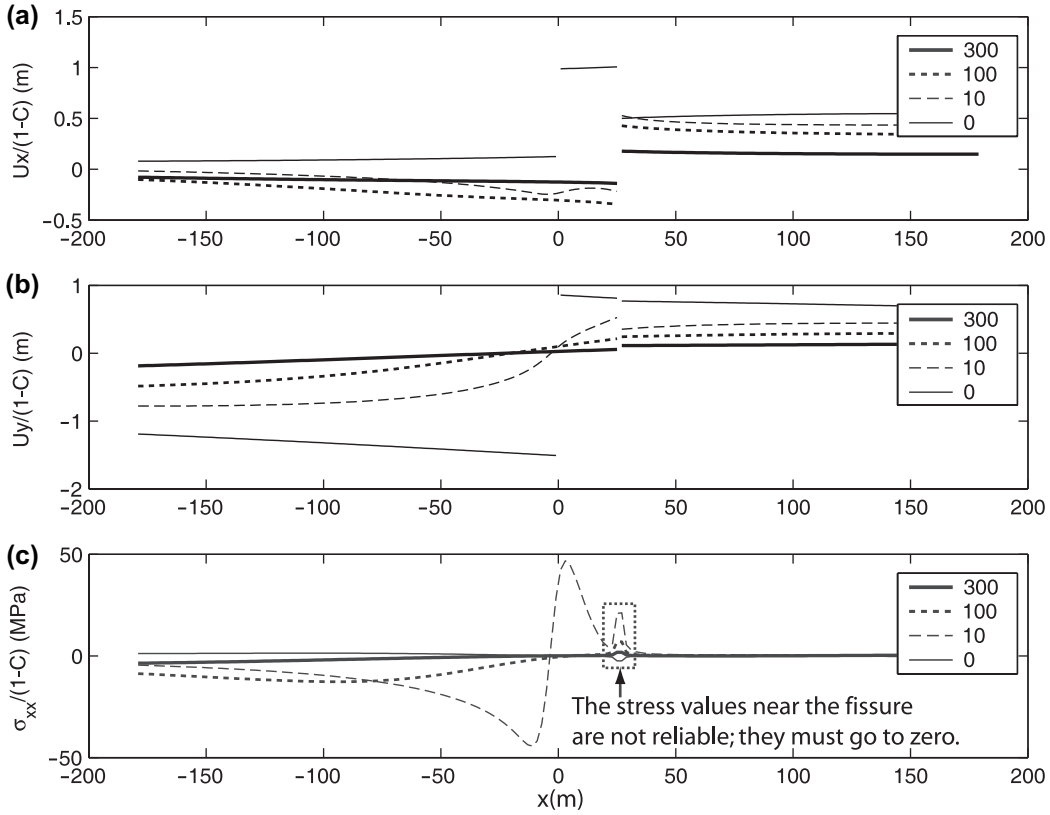

Fig. 12. Displacements and stresses at the surface for a two-component model with a normal fault dipping 70° and a vertical fissure. The curves show results for normal faults with the upper tip at various distances down dip from the surface: 300, 100, 10, and 0 m. (a) Horizontal displacement. (b) Vertical displacement. (c) Horizontal stress perpendicular to fault strike (tension is positive). The minor peaks in stress values near the fissure are artifacts of the numerical modeling.

and intersects the main fault at a down-dip distance of 50 m. All elements are free of shear tractions, and the fissure and antithetic fault are free of normal tractions too. Fig. 13 shows test results for antithetic faults of four lengths: 10, 20, 30, and 40 m. The displacements resemble those for a blind master fault with an upper tip 10 m down-dip from the surface (Fig. 12), but the stresses differ. As the antithetic fault becomes longer and its upper tip approaches the surface, a tension develops on the surface of the hanging wall of the master fault (Fig. 13c). This could explain the presence of the fine fissures we document on the hanging wall of the Ohale fault (Fig. 2).

4.6. Surface displacements

The observed surface throw across the Ohale fault and the observed footwall fissure apertures exceed the model predictions by a factor of ~3, assuming C=0. The model displacements cannot be increased by decreasing the shear strength of the fault, for that is already zero. We consider four other scenarios that might permit the model to match the observed slip: (1) extending the Ohale fault down-dip more than a kilometer; (2) increasing the ambient horizontal tensile stresses; (3) accounting for interaction of the Ohale fault with the Kalanaokuaiki fault; and (4) lowering the elastic modulus. We rule out scenario (1) for two reasons: (a) if the Ohale fault extended further down-dip it would have to cross the much longer Kalanaokuaiki fault (assuming both had a dip of 70°); and (b) the ratio of the trace length of the Ohale fault to its down-dip extent would drop below 2, so the fault shape would be inconsistent with the findings of Nicol et al. (1996). Scenario (2) conflicts with the observation that the fissures near the Ohale fault are not propagating. For a fissure 100 m long not to propagate in rock with a fracture toughness of 1 MPa/m$^{1/2}$, the ambient tensile stress normal to the fissure could not exceed 0.1 MPa. This level is too small to produce the observed scarp heights, so scenario (2) is rejected. To test scenario (3) we modeled the Ohale fault as antithetic to a master Kalanaokuaiki fault, with the faults extending down-dip from the surface at 70° and intersecting. Again, the faults are modeled as supporting no shear tractions and their walls stay in contact. Fig. 14 shows the model slip on both faults for master faults of different down-dip extent. The slip on a frictionless master fault with a down-dip extent greater than 3 km exceeds 20 m (Fig. 14a), the approximate height of the Kalanaokuaiki fault (Duffield, 1975). For a master fault extent between 1.2 and 4 km, the model slip on the Ohale fault at the surface exceeds 3 m (Fig. 14b), the approximate amount for an isolated model fault (Fig. 8b). The peak slip at the surface, 6.4 m, occurs for a master fault extent of 1.2–1.6 km, but this is still ~30% less than observed value. So although fault interaction can substantially enhance slip, interaction by itself appears insufficient to account for the observations. For scenario (4) to be viable, the modulus of the rock

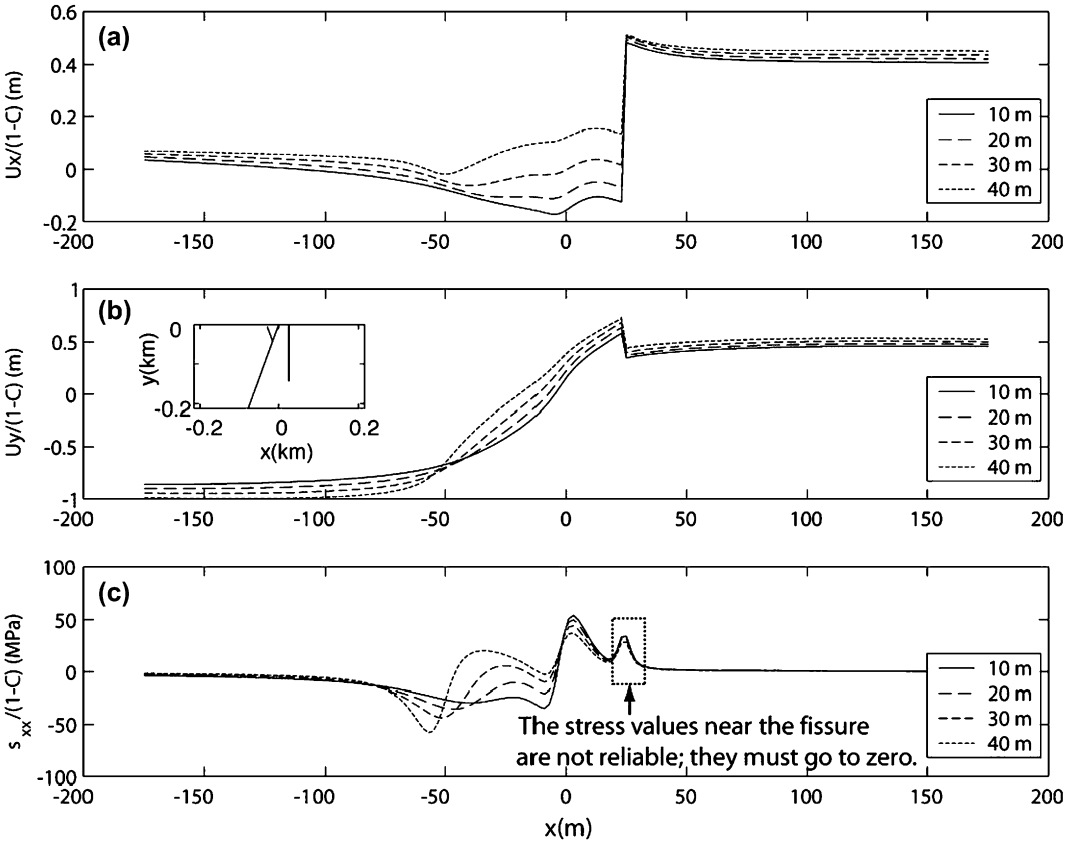

Fig. 13. Displacements and stresses at the surface for a three-component model with a blind master normal fault dipping 70°, a vertical fissure, and a blind antithetic normal fault. The inset in (b) shows the geometry of these features. Calculations are for the upper tip of the antithetic fault at various down-dip extents: 10, 20, 30, and 40 m. The upper tip of the master fault is 5 m down-dip from the surface. (a) Horizontal displacement. (b) Vertical displacement. (c) Horizontal stress perpendicular to fault strike (tension is positive). The minor peaks in stress values near the fissure are artifacts of the numerical modeling. The inset in (b) shows the geometry of the faults and fissures.

would need to decrease by a factor of 3 from its current model level of 5 GPa if the fault were frictionless, and by more if the fault exhibits frictional resistance to slip. Some combination involving an in situ Young's modulus below 5 GPa and fault interaction seems likely to account for the observations.

5. Model for fault propagation along-dip

Based on our field observations of the Ohale fault and our mechanical analyses, we infer the following growth process for a fault that propagates up towards the surface in basalt (Fig. 15):

1. With slip at depth (Fig. 15a), monoclinal flexing of the surface begins and pre-existing cooling joints preferentially open on the footwall where horizontal tensile stresses are highest. Cavities begin to nucleate on the hanging wall side of the fault tip when the near-tip stress perturbation overcomes the ambient vertical compressive stress.
2. As the fault continues to propagate upwards (Fig. 15b), the monocline steepens, fissures on the footwall widen and deepen, and the hanging wall cavity near the fault tip grows. Based on our observations, the widest footwall fissures are at least 20 m deep, and our modeling indicates they could be at least several tens of meters deep.
3. As the fault and fissure overlap at depth (Fig. 15c), horizontal compressive stresses develop in the footwall, but debris that has fallen into the fissure prevents the closure that would otherwise occur as the fault tip approaches the surface. Opening of the fissure increases the compressive stress on the hanging wall near the scarp base, enhancing the tendency for buckling there. Horizontal flow boundaries and vesicle horizons delaminate above the fault tip cavity such that the monocline becomes a monoclinal bridge.
4. As the fault breaches the surface (Fig. 15d), the monoclinal bridge collapses into the underlying cavity, leaving the scarp strewn with broken debris. The rock between the fault and the fissure tilts away from the fissure and subsides slightly.
5. As slip increases, the central limb of the monocline (if it still exists) steepens, and antithetic faulting and fracturing in the subsurface of the hanging wall develops, resulting in fissures on the surface (Fig. 15e). Antithetic faulting could also occur in the stage of Fig. 15d.
6. The footwall fissure becomes linked to the fault, transferring the monocline (if it still exists) to the hanging wall of the fault (Fig. 15f).

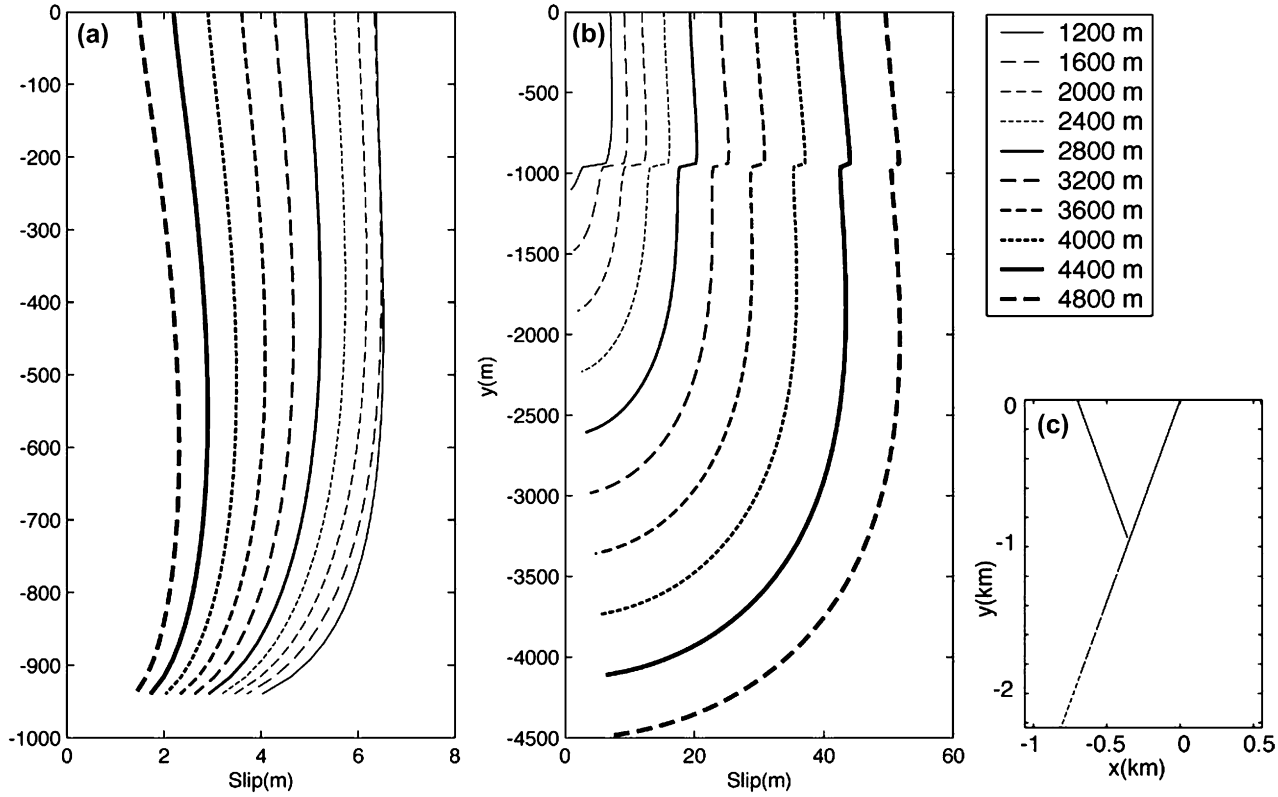

Fig. 14. Slip along an antithetic fault that dips 70° and a master fault that dips 70°, for master fault down-dip extents of 1200–4800 m. The antithetic fault extends 1025 m down-dip from the ground surface to the master fault. The ambient horizontal normal stress is zero (i.e. C=0). (a) Slip along the antithetic fault. (b) Slip along the master fault. (c) Geometry of the antithetic fault and (upper part of) the master fault.

Features analogous to those described here occur in experimental models of normal faults in clay and have been inferred in sedimentary rocks in seismic cross sections (Withjack et al., 1990). Bruhn et al. (1994) also described abundant steeply dipping opening-mode fractures near the surface in the footwalls of normal faults in granitic rock. Our results could shed light on how damage zones (Caine et al., 1996) develop along many normal faults, and not just those in basalt.

6. Discussion

Our concept of how the faults breach the surface is generally consistent with the ideas of Macdonald (1957), Duffield (1975), and Peacock and Parfitt (2002) in that it involves the breaching of a fractured monocline. Our work indicates that the gaping fissures are initially distinct from the faults, although as faulting progresses the fissures begin to become incorporated in a normal fault system, as noted by Duffield (1975) and by Peacock and Parfitt (2002). These gaping fissures could open even if the underlying fault does not open as it slips. We also find that although the buckling is primarily due to the upward propagation of the fault, opening of the footwall fissures promotes the formation of hanging wall buckles, and that the opening of cavities and the stoping of blocks from the walls of the fissures play a key role in the way the system develop; neither Macdonald (1957), Duffield (1975), nor Peacock and Parfitt (2002) identified these processes.

The process of Fig. 15 differs from that proposed by Grant and Kattenhorn (2004) in their study of Icelandic normal faults with scarps more than 10 m tall. They document faults with a vertical scarp along an open gaping fissure at the upper hinge line of a monocline. They considered these scarps to form as a vertical opening mode fracture propagated up to the surface from the tip of a blind normal fault. The process of Fig. 15, however, in which a fissure propagates down from the surface and eventually links with a normal fault at depth, could also yield a fault scarp with the Icelandic attributes. The Kalanaokuaiki fault, the largest fault in the Koae fault system, has characteristics common to both the Ohale fault (e.g. gaping fissures near the top of the scarp, buckles near the fault scarp base, cavities along the scarp, and fissures on the hanging walls) and the Icelandic faults (e.g. gaping fissures near the upper hinge of a monocline). The common elements suggest that a common process is at work. An examination of small scarps in Iceland could test whether our model is applicable there.

Our two-dimensional analyses indicate that the observed footwall fissures, hanging wall buckles, scarp cavities, and monoclines are consistent with normal faults that grow up towards the surface and inconsistent with normal faults that grow down from the surface, but are they diagnostic of upward growth? In their three-dimensional analyses of normal faults that breach the surface, Crider and Pollard (1998) considered semi-elliptical faults with a concave up tip line. Such a shape

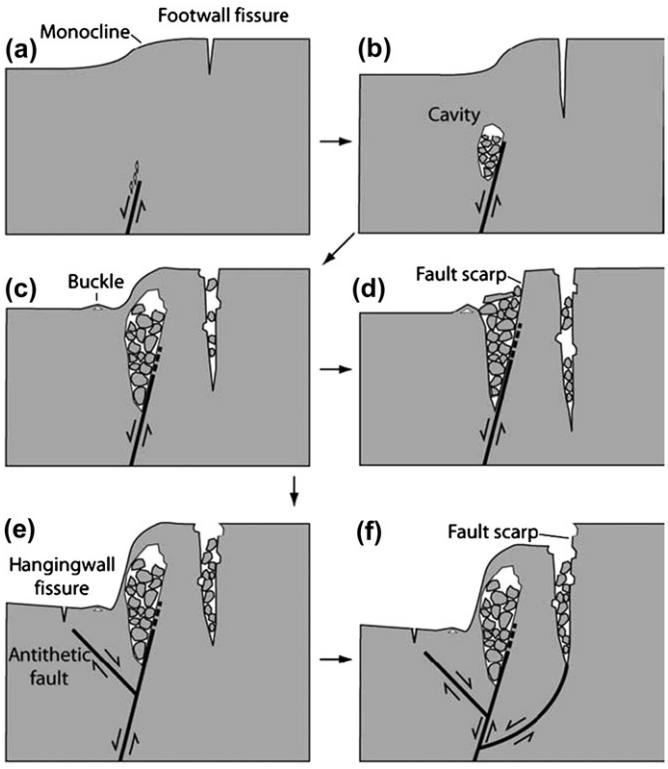

Fig. 15. Conceptual model of the propagation of a normal fault to the surface. The figure does not show effects of resurfacing by lava flows. Stages (a)–(d) occur along the Ohale fault, and stages (e) and (f) are inferred based on observations along the Kalanaokuaiki fault. (a) Slip at depth yields a broad flexure of the surface, opening of pre-existing cooling cracks at the surface, and opening of fractures near the fault tip. (b) As the fault tip propagates towards the surface, cavities open on the hanging wall near the fault tip, and surface fissures widen and deepen. (c) The cavity has grown such that a monoclinal bridge forms. Stoped blocks from the walls of the fissure lodge in the fissure. A buckle begins to develop on the hanging wall near the base of the scarp. (d) The fault breaches the surface and the monoclinal bridge collapses. The fissure remains open owing to the stoped blocks and now accommodates a small amount of dip-slip. (e) If the monoclinal bridge does not collapse, the central limb of the monocline becomes progressively steeper. (f) The gaping fissure links with the fault, transferring the monocline (if still present) to the fault footwall.

is common for opening cracks that nucleate at a surface (Broek, 1982). Subsequent elastic analyses by Kaven (2004) show that monoclinal flexures should develop at the surface past the trace ends of such a semi-elliptical fault. This raises the question of whether fissures such as those along the Ohale fault might have developed by the downward growth of a semi-elliptical normal fault that is also propagating laterally and cutting earlier-formed, fractured fault-end monoclines. We contend that this is unlikely. Our two-dimensional analyses show that normal faults that extend down from the surface would tend to close footwall fissures, so if the Ohale fissures were formed near the fault trace end, they should tend to have maximum apertures near the fault trace end and to become progressively closed towards the fault trace center. Our field observations show, however, that the footwall fissures increase in number and aperture from the east end of the fault trace towards its center (Fig. 2). We conclude that systems of normal faults and footwall fissures with characteristics like those of the Ohale fault are diagnostic of normal faults that have grown up towards the surface.

Non-elastic deformation has several mechanical consequences. For example, the opening of fissures on the footwall enhances the compressive stress on the hanging wall near the eventual fault trace and enhances the tendency for buckling there. The opening of fissures and cavities, and their subsequent choking by debris, prevents a complete elastic rebound once a fault breeches the surface. Non-elastic deformation explains why the height of a scarp is less, and in some cases much less, than the total vertical separation of the ground surface across a fault. Lin and Parmentier (1988) suggested that near-fault deformation known as 'fault drag' might be associated with a fault tip stress concentration. We interpret the flexure of the ground surface on the footwall of the Ohale fault and the associated fractures as non-elastic deformation of this sort.

The non-elastic deformation also can play a key role in fault hydrology. In particular, the fissures, cavities, and scarp rubble contain a loose assortment of large talus blocks and can develop high hydraulic conductivities parallel to fault strike. The hydraulic conductivities of features such as these probably would are more like that of gravel (K_g) than dense basalt (K_{db}) or 'fractured, weathered, or brecciated basalt' (K_{bb}), where $K_g=10^{-3}-10^{0}$ m/s, $K_{db}=10^{-11}-10^{-8}$ m/s, and $K_{bb}=10^{-9}-10^{-5}$ m/s (Freeze and Cherry, 1979). The gravel values are consistent with bulk hydraulic conductivities as high as 3×10^{-2} m/s in a 'zone of potential tension cracks' in basalt at the Idaho Engineering and Environmental Laboratory (Kuntz et al., 2002). The effect of the fissures can be looked at another way. For laminar flow though an open fracture, the volumetric flow rate varies as the cube of fracture aperture (e.g. Gudmundsson, 2000), so an open fracture with an aperture of 2 m permits a volumetric flow rate eight billion times greater than a fracture with an aperture of 1 mm. Furthermore, the cavities, scarp rubble, and fissures can maintain a high hydraulic conductivity even if subsequently overrun by lava. For example, in some places lava flowed against fault scarp rubble and solidified against it, leaving cavernous voids amidst the rubble unfilled. We also have observed lava flows on Mauna Loa that extend across open fissures, rather than flowing into them. Some of these 'bridged' fissures have apertures of several centimeters. Whelan et al. (2002) also document this phenomenon in basalts of the Snake River Plain. These findings collectively indicate that non-elastic deformation along normal fault scarps could have an enormous hydrologic impact.

Footwall fissures and hanging wall buckles develop in alluvium during historic earthquakes along normal faults (e.g. Gianella and Callaghan, 1934; Crone et al., 1987) but apparently are rare. The occurrence of these features demonstrates that they can form in a single earthquake where a fault ruptures up to the surface, but their scarcity suggests that alluvium does not lend itself to either their formation or preservation. The mechanical character of the surface thus greatly influences the type of structures that can be preserved.

Planetary geologists might use our findings in several ways. For example, the abundance of footwall fractures along normal faults could be used to distinguish basaltic ejecta from in situ basalt flows. Aligned pit craters on Mars considered to form in granular materials above dilatant normal faults (Ferrill et al., 2004; Wyrick et al., 2004) might instead develop above footwall fissures. MOLA topographic data, which reflect whether Martian grabens are underlain by dikes (Schultz et al., 2004), could also be used to infer whether Martian faults propagated down from a basaltic bedrock surface or up to it (e.g. Fig. 8a). Since planetary geologists use surface throw distributions to infer how faults grow (e.g. Schultz, 1997), they should be aware that the surface throw along faults with incipient scarps can exceed the scarp height by a factor of three. Our results also bear on the hydrogeology along Martian normal fault systems as well as those on Earth (e.g. Wyrick et al., 2004).

7. Conclusions

Pronounced non-elastic deformation accompanies the propagation of normal faults to the surface in basalt on Kilauea volcano. Scarps of the Koae fault system consistently display locally breached monoclines underlain by prominent cavities. Deep gaping fissures on the footwall, finer fissures on the hanging wall, and buckles at the scarp base parallel the fault trace. The monoclines indicate that the faults propagated up towards the surface rather than down from it. Two-dimensional elastic boundary element analyses for planar blind normal faults with dips greater than 60° yield a tensile stress concentration at the surface of the footwall, where gaping fissures occur, and a compressive stress concentration on the hanging wall at the scarp base, where buckles occur. The surficial tensile stress concentration indicates that the footfall fissures grow down from the surface. A stronger tensile stress concentration develops in the subsurface near the tip of a blind fault on the hanging wall. We infer from this that the cavities initiate at depth near the fault tip and propagate with it up towards the surface. The hanging wall fissures can open in response to slip on a blind antithetic fault with an upper tip near the surface. Stoped blocks derived from walls of footwall fissures help prop the fissures open as a normal fault breaches the surface. The footwall fissures link with the faults as the scarps grow. Fissures, cavities, and scarp rubble provide highly conductive hydraulic pathways along such a normal fault system. We find that information on small scarps is useful in understanding how faults propagate to the surface and for understanding how large scarps form, because many features formed early in scarp development are later overprinted or destroyed.

Acknowledgements

We thank the following reviewers for their comments and constructive criticisms of various drafts of the manuscript: Larry Mastin, Scott Rowland, Paul Wessel, Scott Wilkins, David Peacock, and Special Editor Richard Schultz. We gratefully acknowledge support from the U.S. Department of Energy Office of Basic Energy Sciences (Grant No. DE-FG03-85ER15525). SJM also thanks the U.S. Geological Survey Cascades Volcano Observatory for providing office space and a stimulating environment for working on the manuscript during a sabbatical leave. This is SOEST contribution no. 5627.

Appendix A. Functions for a half-space solution

Solution of the shear and normal displacement discontinuities across boundary elements in a semi-infinite elastic continuum requires modification of the COEFF subroutine in the infinite body code TWODD (Crouch and Starfield, 1983). COEFF calculates the stresses and displacement perturbations (or influence coefficients) induced at observation points by unit shear and normal displacement discontinuities along the boundary elements. The half-space version of COEFF requires nine functions to calculate the influence coefficients as opposed to seven functions for the full-space version. The two extra functions are derived from partial derivatives of the sixth and seventh influence functions of Crouch and Starfield (1983):

$$F8(x,y) = \frac{\partial F6}{\partial y} = \frac{\partial F7}{\partial x}$$
$$F9(x,y) = \frac{\partial F7}{\partial y} \tag{A.1}$$

The sixth and seventh influence functions are:

$$F6(x,y) = \frac{1}{4\pi(1-\nu)}\left(\frac{(x-a)^2-y^2}{((x-a)^2+y^2)^2} - \frac{(x+a)^2-y^2}{((x+a)^2+y^2)^2}\right)$$
$$F7(x,y) = \frac{2y}{4\pi(1-\nu)}\left(\frac{(x-a)}{((x-a)^2+y^2)^2} - \frac{(x+a)}{((x+a)^2+y^2)^2}\right) \tag{A.2}$$

These equations yield F8 and F9:

$$F8(x,y) = \frac{2y}{4\pi(1-\nu)}\left[\frac{y^2-3(x-a)^2}{((x-a)^2+y^2)^3} - \frac{y^2-3(x+a)^2}{((x+a)^2+y^2)^3}\right] \tag{A.3}$$

$$F9(x,y) = \frac{2}{4\pi(1-\nu)}\left[\frac{(x-a)((x-a)^2-3y^2)}{((x-a)^2+y^2)^3} - \frac{(x+a)((x+a)^2-3y^2)}{((x+a)^2+y^2)^3}\right] \tag{A.4}$$

References

Atkinson, B.K., Meredith, P.G., 1987. Experimental fracture mechanics data for rocks and minerals. In: Atkinson, B.K. (Ed.), Fracture Mechanics of Rock. Academic Press, London, pp. 477–525.

Bailey, R.A., Dalrymple, G.B., Lanphere, M.A., 1976. Volcanism, structure and geochronology of the Long Valley caldera, Mono County, California. Journal of Geophysical Research 81, 725–744.

Bandfield, J.L., Hamilton, V.E., Christensen, P.R., 2000. A global view of Martian surface compositions from MGS-TES. Science 287, 1626–1630.

Broek, D., 1982. Elementary Engineering Fracture Mechanics. Martinus Nijhoff, The Netherlands.

Bruhn, R.L., Schultz, R.A., 1996. Geometry and slip distribution in normal fault systems: implications for mechanics and fault-related hazards. Journal of Geophysical Research 101, 3401–3412.

Bruhn, R.L., Parry, W.T., Yonkee, W.A., Thompson, T., 1994. Fracturing and hydrothermal alteration in normal fault zones. Pure and Applied Geophysics 142, 609–644.

Caine, J.S., Evans, J.P., Forster, C.B., 1996. Fault zone architecture and permeability structure. Geology 24, 1025–1028.

Carillo, M.M., 1998. Normal faulting in the Pathe geothermal area, Central Mexico. Geofisica Internacional 37, 103–111.

Christensen, P.R., Bandfield, J.L., Bell III, J.F., Gorelick, N., Hamilton, V.E., Ivanov, A., Jakosky, B.M., Kieffer, H.H., Lane, M.D., Malin, M.C., McConnochie, T., McEwen, A.S., McSween Jr., H.Y., Mehall, G.L., Moersch, J.E., Nealson, K.H., Rice Jr., J.W., Richardson, M.I., Ruff, S.W., Smith, M.D., Titus, T.N., Wyatt, M.B., 2003. Morphology and composition of the surface of Mars: Mars Odyssey THEMIS results. Science 300, 2056–2061.

Cooke, M.L., Pollard, D.D., 1997. Bedding-plane slip in initial stages of fault related folding. Journal of Structural Geology 19, 567–580.

Crider, J.G., Pollard, D.D., 1998. Fault linkage: three-dimensional mechanical interaction between échelon normal faults. Journal of Geophysical Research 103, 24,373–24,391.

Crone, A.J., Machette, M.N., Bonilla, M.G., Lienkaemper, J.J., Pierce, K.L., William, E., Scott, W.E., Bucknam, R.C., 1987. Surface faulting accompanying the Borah Peak earthquake and segmentation of the Lost River Fault, central Idaho. Bulletin of the Seismological Society of America 77, 739–770.

Crouch, S.L., Starfield, A.M., 1983. Boundary Element Methods in Solid Mechanics. Allen and Unwin, London.

Delaney, P.T., Miklius, A., Arnadottir, T., Okamura, A.T., Sako, M.K., 1993. Motion of Kilauea Volcano during sustained eruption from the Puu Oó and Kupaianaha vents, 1983–1991. Journal of Geophysical Research 98, 17,801–17,820.

Duffield, W.A., 1975. Structure and origin of the Koae fault system, Kilauea Volcano, Hawaii. United States Geological Survey, Professional Paper 856.

Duffield, W.A., Bacon, C.R., Dalrymple, G.B., 1980. Late Cenozoic volcanism, geochronology, and structure of the Coso Range, Inyo County, California. Journal of Geophysical Research 85, 2381–2404.

Engelder, T., 1993. Stress Regimes in the Lithosphere. Princeton University Press, Princeton, New Jersey.

Ferrill, D.A., Morris, A.P., 2001. Displacement gradient and deformation in normal fault systems. Journal of Structural Geology 23, 619–638.

Ferrill, D.A., Wyrick, D.Y., Morris, A.P., Sims, D.W., Franklin, N.M., 2004. Dilational fault slip and pit chain formation on Mars. GSA Today 14, 4–12.

Fiske, R.S., Koyanagi, R.Y., 1968. The December 1965 eruption of Kilauea Volcano, Hawaii. United States Geological Survey, Professional Paper 607.

Freeze, R.A., Cherry, J., 1979. Groundwater. Prentice-Hall, Englewood Cliffs, New Jersey.

Gianella, V.P., Callaghan, E., 1934. The Cedar Mountain, Nevada, earthquake of December 20, 1932. Seismological Society of America Bulletin 24, 345–377.

Grant, J.V., Kattenhorn, S.A., 2004. Evolution of vertical faults at an extensional plate boundary, southwest Iceland. Journal of Structural Geology 26, 1579–1593.

Gudmundsson, A., 2000. Fracture dimensions, displacements and fluid transport. Journal of Structural Geology 22, 1221–1231.

Head III, J.W., Wilson, L., 1993. Lunar graben formation due to near-surface deformation accompanying dike emplacement. Planetary Science 41, 719–727.

Head III, J.W., Crumpler, L.S., Aubele, J.C., Guest, J., Saunders, R.S., 1992. Venus volcanism: classification of volcanic features and structures, associations, and global distribution for Magellan data. Journal of Geophysical Research 97, 13,153–13,197.

Hiesinger, H., Head III, J.W., Wolf, U., Jaumann, R., Neukum, G., 2003. Ages and stratigraphy of mare basalts in Oceanus Procellarum, Mare Nubium, Mare Cognitum, and Mare Insularum. Journal of Geophysical Research 108, 5065, doi:10.1029/2002JE001985.

Kattenhorn, S.A., Pollard, D.D., 1999. Is lithostatic loading important for the slip behavior and evolution of normal faults in the Earth's crust? Journal of Geophysical Research 104, 28,879–28,898.

Kaven, J.O., 2004. Normal fault growth in three dimensions. M.S. thesis, University of Hawaii.

Kelley, D.S., Baross, J.A., Delaney, J.R., 2002. Volcanoes, fluids, and life at mid-ocean ridge spreading centers. Annual Review of Earth and Planetary Sciences 30, 385–491.

Kinoshita, W.T., 1968. May 1963 earthquakes and deformation in the Koae fault zone, Kilauea Volcano, Hawaii. United States Geological Survey, Professional Paper 575-C, pp. C173–C176.

Kinoshita, W.T., Krivoy, H.L., Mabey, D.R., MacDonald, R.R., 1963. Gravity survey of the island of Hawaii. United States Geological Survey, Professional Paper 475-C, pp. C115–C116.

Kuntz, M.A., Anderson, S.R., Champion, D.E., Lanphere, M.A., Grunwald, D.J., 2002, Tension cracks, eruptive fissures, dikes, and faults related to late Pleistocene–Holocene basaltic volcanism and implications for the distribution of hydraulic conductivity in the eastern Snake River Plain, Idaho. In: Link, P.K., Mink, L.L. (Eds.), Geology, Hydrogeology, and Environmental Remediation. Idaho National Engineering and Environmental Laboratory, Eastern Snake River Plain, Idaho. Geological Society of America Special Paper 353, pp. 111–133.

Lin, J., Parmentier, E.M., 1988. Quasistatic propagation of a normal fault: a fracture mechanics model. Journal of Structural Geology 10, 249–262.

Link, P.K., Mink, L.L. (Eds.), 2002. Geology, Hydrogeology, and Environmental Remediation. Idaho National Engineering and Environmental Laboratory, Eastern Snake River Plain, Idaho. Geological Society of America Special Paper 353.

Lipman, P.W., Lockwood, J.P., Okamura, R.T., Swanson, D.A., Yamashita, K.M., 1985. Ground deformation associated with the 1975 magnitude 7.2 earthquake and resulting changes in activity of Kilauea Volcano, Hawaii. United States Geological Survey, Professional Paper 1276.

Macdonald, G.A., 1957. Faults and monoclines on Kilauea Volcano, Hawaii. Geological Society of America Bulletin 68, 269–271.

Martel, S.J., 2000. Modeling elastic stresses in long ridges with the displacement discontinuity method. Pure and Applied Geophysics 157, 1039–1057.

Martel, S.J., Muller, J., 2000. A two-dimensional boundary element method for calculating elastic gravitational stresses in slopes. Pure and Applied Geophysics 157, 989–1007.

McGarr, A., Gay, N.C., 1978. State of stress in the Earth's crust. Annual Review of Earth and Planetary Science 6, 405–436.

Nicol, A., Watterson, J., Walsh, J.J., Childs, C., 1996. The shapes, major axis orientations and displacement patterns of fault surfaces. Journal of Structural Geology 18, 235–248.

Olson, J., Pollard, D.D., 1989. Inferring paleostresses from natural fracture patterns: a new method. Geology 17, 345–348.

Owen, S., Segall, P., Freymueller, J., Miklius, A., Denlinger, R., Arnadottir, T., Sako, M., Bürgmann, R., 1995. Rapid deformation of the south flank of Kilauea Volcano, Hawaii. Science 267, 1328–1332.

Peacock, D.C.P., Parfitt, E.A., 2002. Active relay ramps and normal fault propagation on Kilauea Volcano, Hawaii. Journal of Structural Geology 24, 729–742.

Pollard, D.D., Segall, P., 1987. Theoretical displacements and stresses near fractures in rock: with applications to fault, joints, veins, dikes, and solution surfaces. In: Atkinson, B.K. (Ed.), Fracture Mechanics of Rock. Academic Press, London, pp. 277–348.

Rubin, A.M., Pollard, D.D., 1987. Origin of blade-like dikes in volcanic rift zones. In: Decker, R.W., Wright, T.L., Stauffer, P.H. (Eds.), Volcanism

in Hawaii. United States Geological Survey Professional Paper 1350, pp. 1549–1570.

Schultz, R.A., 1993. Brittle strength of basaltic rock masses with applications to Venus. Journal of Geophysical Research 98, 10,883–10,895.

Schultz, R.A., 1997. Displacement–length scaling for terrestrial and Martian faults: implications for Valles Marineris and shallow planetary grabens. Journal of Geophysical Research 102, 12,009–12,015.

Schultz, R.A., Okubo, C.H., Goudy, C.L., Wilkins, S.J., 2004. Igneous dikes on Mars revealed by Mars Orbiter Laser Altimetry topography. Geology 32, 889–892.

Singleton, M.J., Criss, R.E., 2002. Effects of normal faulting on fluid flow in an ore-producing hydrothermal system, Comstock Lode, Nevada. Journal of Volcanology and Geothermal Research 115, 437–450.

Solomon, S.C., Smrekar, S.E., Bindschlader, D.L., Grimm, R.E., Kaula, W.M., McGill, G.E., Phillips, R.J., Saunders, R.S., Schubert, G., Squyres, S.W., Stofan, E.R., 1992. Venus tectonics: an overview of Magellan observations. Journal of Geophysical Research 97, 13,199–13,255.

Strom, R.G., 1987. Mercury: The Elusive Planet. Smithsonian Institution Press, Washington, D.C.

Swanson, D.A., Duffield, W.A., Fiske, R.S., 1976. Displacement of the south flank of Kilauea Volcano: the result of forceful intrusion of magma into the rift zones. United States Geological Survey Professional Paper 963.

Turcotte, D.L., Schubert, G., 1982. Geodynamics: Applications of Continuum Physics to Geological Problems. John Wiley & Sons, New York.

Whelan, J.A., Johannesen, C.M., Reeves, K.S., Clemo, T.M., Glover, J.A. Bosworth K.W., 2002. Morphology of inflated pahoehoe lavas and spatial architecture of their porous and permeable zones, eastern Snake River Plain, Idaho. In: Link, P.K., Mink, L.L. (Eds.), Geology, Hydrogeology, and Environmental Remediation. Idaho National Engineering and Environmental Laboratory, Eastern Snake River Plain, Idaho. Geological Society of America Special Paper 353, pp. 135–150.

Willemse, E.J.M., 1997. Segmented normal faults: correspondence between three-dimensional mechanical models and field data. Journal of Geophysical Research 102, 675–692.

Willemse, E.J.M., Pollard, D.D., Aydin, A., 1996. Three-dimensional analyses of slip distributions on normal fault arrays with consequences for fault scaling. Journal of Structural Geology 18, 295–309.

Wilson, J.E., Goodwin, L.B., Lewis, C.J., 2003. Deformation bands in non-welded ignimbrites: petrophysical controls on fault-zone deformation and evidence of preferential fluid flow. Geology 31, 837–840.

Withjack, M.O., Olson, J., Peterson, E., 1990. Experimental models of extensional forced folds. American Association of Petroleum Geologists Bulletin 74, 1038–1054.

Wolfe, E.W., Morris, J., 1996. Geologic map of the island of Hawaii. United States Geological Survey Map, I-2524-A.

Wyrick, D., Ferrill, D.A., Morris, A.P., Colton, S.L., Sims, D.W., 2004. Distribution, morphology, and origins of Martian pit crater chains. Journal of Geophysical Research 109, E06005, doi:10.1029/2004JE002240.